Acta Materialia 164 (2019) 135–152

Contents lists available at ScienceDirect

Acta Materialia

journal homepage: www.elsevier.com/locate/actamat

Full length article

In situ tension-tension strain path changes of cold-rolled Mg AZ31B

K. Sofinowski [a, b], T. Panzner [a], M. Kubenova [a], J. Čapek [c], S. Van Petegem [a], H. Van Swygenhoven [a, b, *]

[a] Paul Scherrer Institut, CH-5232 Villigen, Switzerland
[b] Neutrons and X-rays for Mechanics of Materials, Institute of Materials (IMX), École Polytechnique Fédérale de Lausanne (EPFL), 1012 Lausanne, Switzerland
[c] Department of Physics of Materials, Faculty of Mathematics and Physics, Charles University, Ke Karlovu 5, 121 16 Prague, Czech Republic

ARTICLE INFO

Article history:
Received 29 May 2018
Received in revised form
5 September 2018
Accepted 16 October 2018
Available online 22 October 2018

Keywords:
Magnesium alloy
In situ tension test
Neutron diffraction
Plastic deformation
Strain path change

ABSTRACT

The mechanical behavior of cold-rolled Mg AZ31B is studied during in-plane multiaxial loading and tension-tension strain path changes performed on cruciform samples using *in situ* neutron diffraction and EBSD. The results are compared with uniaxial tension loading of dogbone-shaped samples measured with *in situ* neutron diffraction and acoustic emission. The activity of slip and twinning mechanisms and the active twin variants are discussed for the different strain paths. It is shown that initial strains of 4–5% cause a strengthened yield stress during reload for strain path change angles of 90 and 135°. The strengthening is primarily due to dislocation accumulation during the initial load impeding dislocation motion during the reload. The twinning observed during the prestrain activates complex multivariant secondary twinning which may also contribute to the strengthening in the reload.

1. Introduction

The widespread use of magnesium and its alloys in lightweight structural elements for the transportation industry has been limited because of their poor formability at room temperature as compared to other ductile metals [1–3]. In particular, the out-of-plane basal texture of cold-rolled sheet greatly limits $\{10\bar{1}2\}$ extension twinning for in-plane tensile loading, the most easily activated mode that can accommodate *c*-axis strain. Instead, high-CRSS $\langle c+a \rangle$ slip on pyramidal planes and non-basal slip of $\langle a \rangle$ dislocations must be activated to provide enough independent slip systems to accommodate strain [4–6]. The result is a highly anisotropic deformation behavior that depends heavily on the loading mode and direction.

In situ neutron diffraction has been used extensively to investigate the evolution of intergranular strain during loading to provide insight on the relative behavior of different magnesium alloy deformation modes. The results have been compared with various crystal plasticity models [7–15]. Muránsky et al. [16] demonstrated the effectiveness of using Schmid Factor (SF) analysis to evaluate the activity of deformation mechanisms in an AZ31B dogbone under uniaxial tension. Čapek et al. [17] used SF analysis to determine the susceptibility of grain orientations to twinning under tensile and compressive loading.

Various other techniques have been used to study, in particular, the interaction between twins and dislocations. In situ acoustic emission (AE) has been used in several studies as a complementary technique to monitor the relative activity of dislocation slip and twinning with a high time resolution [18–20]. Electron backscatter diffraction (EBSD) and transmission electron microscopy (TEM) studies have revealed the influence of texture on dislocation slip [21,22], twin-twin interactions [23], and the interactions between twinning and dislocations [24–31]. Notably, Lou et al. [32] used AE and EBSD to show that the activation stress for nucleation of twins is less than that of de-twinning in AZ31B. Wagoner et al. [33] showed that the hardening contribution of tension twinning can be ascribed more to textural hardening rather than the twins acting as barriers for dislocation slip.

Although it is widely accepted that deformation mechanisms depend heavily on load path, all of the aforementioned works have been restricted to uniaxial tension and compression. Little attention has been given to tension-tension load path changes or multiaxial loads that occur in cold-forming operations of AZ31 sheet. Chino et al. [34] examined uniaxial and biaxial tensile

* Corresponding author. Paul Scherrer Institut, CH-5232 Villigen, Switzerland.
E-mail address: helena.vs@psi.ch (H. Van Swygenhoven).

https://doi.org/10.1016/j.actamat.2018.10.033

loading using EBSD and TEM. They observed an increased stretch formability for larger grain sizes which was attributed to enhanced basal slip due to lattice rotation by twinning. Steglich et al. [35] used the mechanical behavior of an in-plane equibiaxial tensile test to modify the VPSC model of Lebensohn and Tomé [36,37]. Their results suggest that for this loading mode the CRSS of prismatic $\langle a \rangle$ slip is actually higher than that of pyramidal $\langle c+a \rangle$ slip, whereas all uniaxial studies have suggested the opposite. Zhang et al. [38] performed a deep drawing experiment and used EBSD analysis to study the effect of texture on the limiting drawing ratio. The groups of Wen et al. [39] and Hama et al. [40] performed the first tension-tension strain path studies by loading a dogbone specimen, cutting smaller dogbones at various angles relative to the previous loading direction, then loading those smaller dogbones uniaxially again. Their results show that back-stresses from dislocation motion in the initial load cause lower yield stresses with increasing strain path change angle. All of these studies, however, were performed *ex situ*, so only the macroscopic stress-strain and texture can be compared. No experimental validation of the specific mechanisms responsible for the deformation are presented.

In this work, the relative activity of deformation modes under in-plane multiaxial tension and strain path changes in Mg AZ31B sheet were studied. Six load paths were performed on cruciform-shaped specimens: three monotonic loads with force ratio (F1:F2) between axis 1 and 2 of 1:0 (uniaxial along the rolling direction), 7:10, and 1:1, and three load path changes in which samples were preloaded along the rolling direction, unloaded, and followed by a second load of 1:0, 7:10, and 1:1. Uniaxial tensile deformation of a dogbone sample was performed for comparison. Samples were measured *in situ* using simultaneous neutron diffraction, digital image correlation (DIC), and (AE). Post-mortem EBSD imaging was used to confirm the results of the neutron diffraction and identify the active twin variants.

2. Material and experimental procedure

2.1. Material and sample geometry

Cold-rolled Mg AZ31B sheet (chemical composition 3.13Al-1.12Zn-0.44Mn-0.025Si wt. %, trace amounts of Fe, Cu, and Ni, balance Mg) was purchased from Concept Métal. EBSD analysis was performed using a Zeiss ULTRA 55 field emission gun scanning electron microscope equipped with an EDAX Hikari Camera and operated at 20 kV in high current mode with an aperture of 120 μm. The EBSD data was analyzed using OIM Analysis 7.3 software. Samples were ground using silicon carbide grinding paper to 1200 grit, then polished with 6, 3 and 1-μm oil-based diamond paste, and finished by polishing with 0.05-μm high purity alumina and colloidal silica. EBSD maps were collected using a step size of 0.3 μm and with field of view of 716 μm × 287 μm.

Fig. 1 shows the (A) (00.2) and (10.0) inverse pole figures (IPF), (B) IPF map, and (C) (00.2) and (10.0) pole figures for the initial microstructure. The IPF map is taken in the out-of-plane direction, but the orientations are colored with respect to the diffraction vector **Q**, i.e. the neutrons "see" the grain orientations in Fig. 1B. The grains are roughly equiaxed with an average grain size of 27 ± 17 μm and there is a strong (00.2) out-of-plane basal texture.

For the mechanical tests, cruciform and dogbone specimens were cut from a 10 mm thick sheet using water jet cutting as in Ref. [41]. The test section was reduced by mechanical grinding to a thickness of 2.5 ± 0.02 mm. Sample dimensions are the same as in Ref. [41].

2.2. Mechanical testing and neutron diffraction

Samples were tested using the multiaxial deformation rig at the POLDI beamline of the Swiss Spallation Source (SINQ). The rig is used to apply proportional and non-proportional loads for in-plane tensile testing of cruciform samples. For more information on the machine specifications and capabilities, see Ref. [41].

Six different load paths were performed with the cruciform samples as shown in Fig. 2. Load paths A-C describe monotonic load paths with no preload, with load ratios F1:F2 between the axes of 1:0 (uniaxial), 1:1 (equibiaxial), and 7:10, respectively. Load paths D-F describe load path changes (LPCs). For all three LPCs, specimens were first loaded and unloaded uniaxially on axis 1 (1:0 load-unload), then reloaded to force values up to 20 kN with load ratios of 0:1, 1:1, and 7:10, respectively. During the uniaxial loads, the "unloaded" axis was held at constant force F = 300 N.

The macroscopic strain is measured using the 3D DIC system Gom Aramis® as described in Ref. [41]. The system uses two 5 megapixel CMOS cameras angled at 15° to the normal of the center of the sample. The cameras measure a 20 × 20 mm^2 field of view. A random speckle pattern is created on each sample by spraying with a fine mist of paint. Images are taken during loading at a frequency of 1 Hz. The macroscopic strain tensor is calculated over a 3.8 × 3.8 mm^2 gauge area at the center of the test section corresponding to the area intersected by the neutron beam. All strain values reported in this work are averaged over this area. From the macroscopic strain tensor ε the equivalent (Von Mises) strain is calculated by:

$$\varepsilon_{Eq} = \frac{1}{1+\upsilon'}\sqrt{\frac{1}{2}\left[(\varepsilon_1-\varepsilon_2)^2+(\varepsilon_2-\varepsilon_3)^2+(\varepsilon_3-\varepsilon_1)^2\right]} \quad (1)$$

where υ' is the effective Poisson's ratio.

Due to the complex cruciform geometry, the stress state at the center of the cruciform samples cannot be directly calculated from the applied load. The circular thickness reduction in the center causes additional stresses due to the geometry of the sample itself, termed the "ring effect" or "cross-talk" between the arms [42,43]. The ring effect can be thought of as adding an additional "geometrical" Poisson contraction to the deformation [41]. Assuming the test section is in a plane stress state, the effect can be measured as the ratio between the strain components along the two principle axes $\varepsilon_2/\varepsilon_1$ for a uniaxial deformation along axis 1. For this cruciform shape and material, this ratio is $\varepsilon_2/\varepsilon_1 = -0.51$ in the elastic regime and in the plastic regime the difference increases to $\varepsilon_2/\varepsilon_1 = -0.80$. For comparison, the Poisson contraction of the dogbone is $\nu = -0.31$ in the elastic regime and $\nu = -0.58$ in the plastic regime. The development of the ring effect with respect to the elastic and plastic regimes is discussed more in depth in Ref. [43].

Neutron diffraction was performed at the POLDI beamline at SINQ (Paul Scherrer Institute, Switzerland) [44,45]. The principles and setup of the beamline are the same as in Ref. [41]. A schematic of the setup and the peak fitting equations using Mantid data analysis software [46] are provided as supplementary material online. The samples are oriented such that the scattering vector **Q** is in-plane with the sample, along horizontal axis 1. Thus, if the cruciform is strained along axis 1, the loading direction is parallel with **Q**. If it is strained along axis 2, the loading direction is perpendicular to **Q**.

All samples were loaded using force control at a rate of 40 N/s. For each load-unload, nine (in some cases eight) points were measured: one initial point, two (or one) points in the elastic

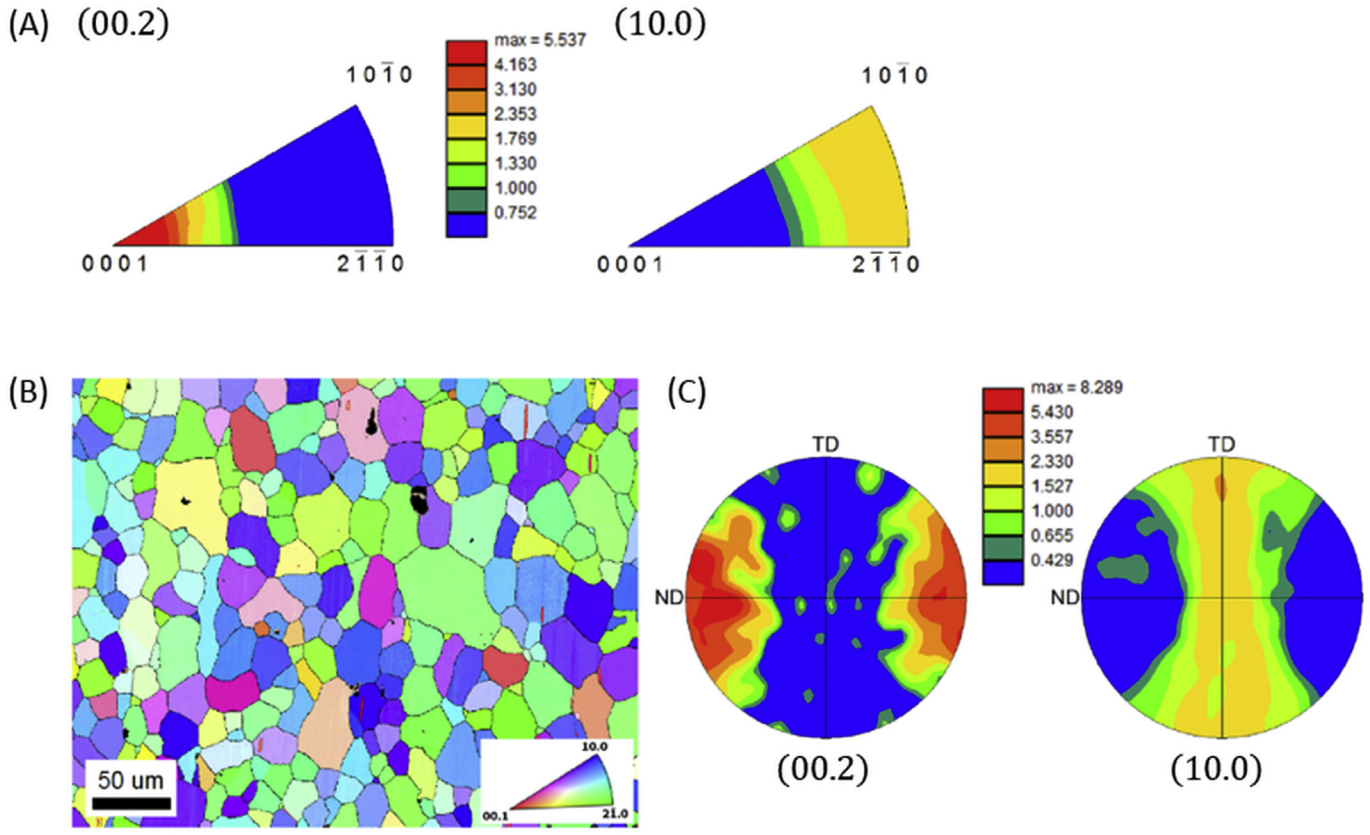

Fig. 1. (A) IPFs, (B) IPF map, and (C) corresponding pole figures of the initial microstructure. The grain orientations in the IPF map are colored with respect to the diffraction vector **Q**.

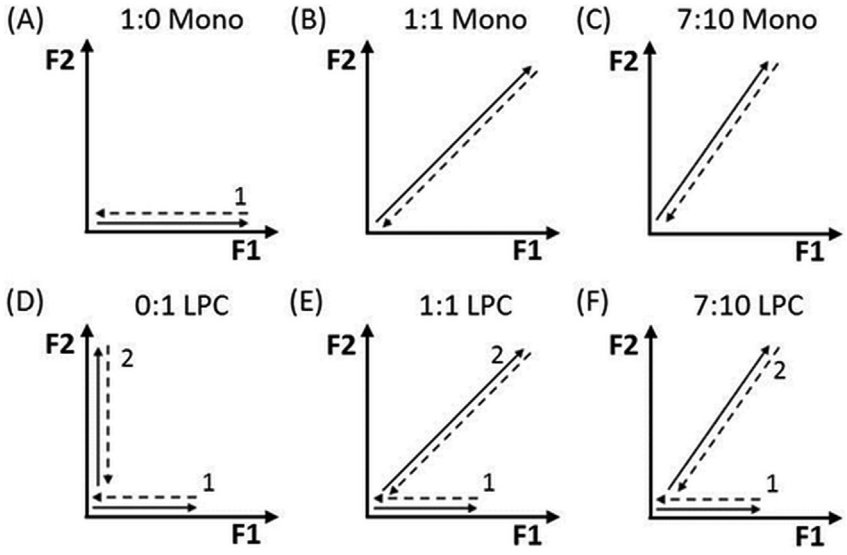

Fig. 2. Diagrams of the load paths. The preload-unload (force ratio F1:F2 = 1:0) is labeled as "1", and the second load-unloads are labeled as "2".

regime, five points in the plastic regime and one point in the completely unloaded state. Each point was measured for 75 min. For measurements in the elastic regime, the sample was held at constant force. For measurements in the plastic regime, the sample was held at constant displacement so as to minimize plastic deformation during the measurements. To mitigate the effect of stress relaxation during measurements, a pause of 300 s was taken at each point before neutron data was collected.

2.3. Acoustic emission

Acoustic emission was measured simultaneously for all samples, dogbone and cruciform, with the neutron diffraction. However, due to the development of stress concentrations in the corner of the cruciform arms, the corners are always at a later stage of deformation than the gauge section. Consequently, it is difficult to separate the signal caused by the corner of the arms from the signal

being measured by the neutrons. Therefore, only the acoustic emission measurements from the dogbone are discussed in this paper. For more details on the acoustic emission setup and data analysis techniques we refer to [20,47].

2.4. Normalized resolved shear stress analysis

The normalized resolved shear stresses (NRSS) were calculated for 1:0, 7:10, and 1:1 loading for all potentially active slip and twinning deformation modes. NRSSs were calculated for all grain families with a lattice plane normal parallel to **Q** (i.e. grains in diffraction condition) using a generalized resolved shear stress law similar to the one described by Muránsky et al. [16]:

$$m = \mathbf{b}^T \cdot \mathbf{g}^T \cdot \mathbf{S} \cdot \mathbf{g} \cdot \mathbf{n} \quad (2)$$

where **b** is the slip burgers vector, **n** is the slip-plane normal, and $\mathbf{g^T S g}$ is the normalized stress tensor **S** in three dimensions expressed in the crystal orientation. For the twinning modes, **b** is the twinning shear direction and **n** is the twin-plane normal. In the special case of uniaxial tension on a dogbone, Eq. (2) yields the Schmid Factor. For multi-slip cases, we will call this value the normalized resolved shear stress. For multiaxial tensile stress states, the maximum value is 0.5. For a stress state with both positive and negative stress components, the maximum value can be up to 1.0 (in the case of pure shear).

NRSS values were calculated for both the initial and prestrained texture. For a given deformation mode and grain family, the maximum NRSS for each slip system of each possible grain orientation contributing to the diffraction was calculated as described schematically in Fig. 3. The NRSS values for each grain family were weighted based on the area fraction of grains in the IPF maps for the initial and prestrained microstructure. A full description of the calculations is provided in the Appendix.

The distribution of NRSS values shows how well a grain family is oriented for each possible deformation mechanism. However, whether or not a given mechanism is active also depends on the critical resolved shear stress (CRSS). A selection of reported CRSS values for AZ31 is shown in Table 1. On average, $CRSS_{Ba\langle a\rangle} \approx CRSS_{TTW}$, $CRSS_{Pri\langle a\rangle} \approx CRSS_{Pyr\langle a\rangle}$ and they are 3–4 times higher than $CRSS_{Ba\langle a\rangle}$, and $CRSS_{Pyr^{2nd}\langle c+a\rangle}$ is 5–6 times higher than $CRSS_{Ba\langle a\rangle}$. Thus, for a higher CRSS mechanism to be activated first, its NRSS values must be significantly higher.

The NRSS distributions for each grain family are used to interpret the lattice strain and integrated intensity obtained by neutron diffraction. This data is measured from a large ensemble of grains. The possibility that different slip systems may be active in individual grains in a grain family is not excluded, but the peak behavior represents the collective response of the ensemble of grains.

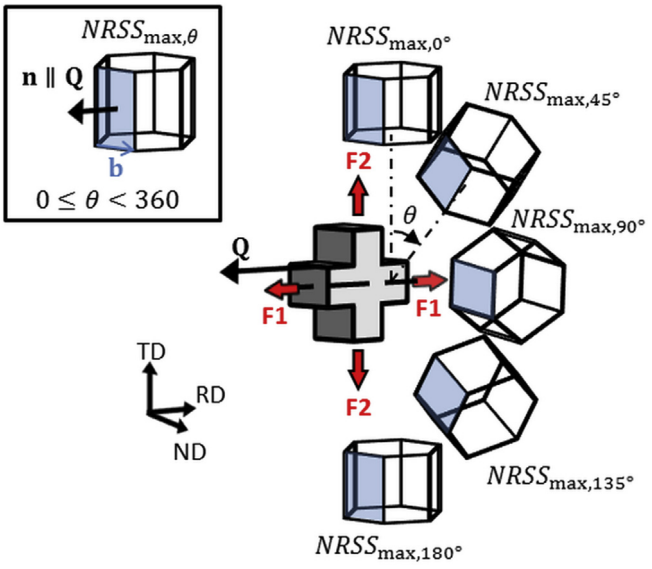

Fig. 3. Schematic showing how the NRSS is calculated for a given slip mechanism and diffracting grain family. (A) The maximum NRSS for a given grain orientation and deformation mode is calculated from all possible slip systems. (B) The process is repeated for each grain contributing to the diffraction peak and the results are weighted by the texture.

3. Results

3.1. Uniaxial deformation (dogbone)

Fig. 4A shows the evolution of the acoustic emission signal as a function of the true stress-true strain curve (black curve). The count rate of the total acoustic emission signal is shown on a logarithmic scale as light grey bars. The relative contributions of the twinning and dislocations to the total acoustic emission signal are shown in red and blue, respectively. At stresses below 150 MPa, the twinning and dislocation contributions do not add up to 100% due to the presence of noise in the signal.

Fig. 4B and C displays the peak evolution of six diffracting grain families as a function of the applied stress. The integrated intensity evolution is shown in Fig. 4B, with values normalized to the initial intensity for each peak. The lattice strain evolution is shown in Fig. 4C. The crosses indicate the residual lattice strain for the grain families after unloading. The vertical lines indicate the 0.02% and 0.2% yield offset.

Table 2 shows the NRSS values for the dogbone for all possible deformation mechanisms. For the dogbone, the direction of the applied stress is parallel to the diffraction vector within the angular range of the detector, so all of the grains that contribute to a given diffraction peak have nearly the same NRSS.

Between 0 and 75 MPa, in the elastic regime, the lattice strain evolution of all grain families is very similar. This is expected given that single crystal pure Mg is elastically isotropic, with an anisotropy factor S_{66}/S_{44} of 0.97 [16]. In this region, the acoustic emission shows that there is no twinning signal and the dislocation signal is small. The integrated intensities of all peaks are relatively stable; however, the {10.0} intensity varies noticeably at stresses before 0.02% yield. Such large variations over a small strain range could be

Table 1
CRSS values from crystal plasticity simulations of AZ31.

Model	CRSS (MPa)				
	$Ba\langle a\rangle$	$Pri\langle a\rangle$	$Pyr\langle a\rangle$	$Pyr^{2nd}\langle c+a\rangle$	TTW
EPSC-TDT, VPSC-TDT [15]	12	75		100	30
T-CPFE [48]	17	108		290	12.8
EVPSC [49]	25	98		315	35
CPFE [40]	25	95		100	40
VPSC [35],[a]	28	110		96	2
EVPSC [14]	17	85		100	20
VPSC (various) [50]	9–21	73–90		100–148	31–38
EPSC [16]	30	85–90	80	95–100	35
VPSC [32]	24	88		160	
EPSC [9]	10	55		60	30
EPSC [9] [b]	20	90	65	95	30

[a] 1:1 proportional loading.
[b] Extrusion.

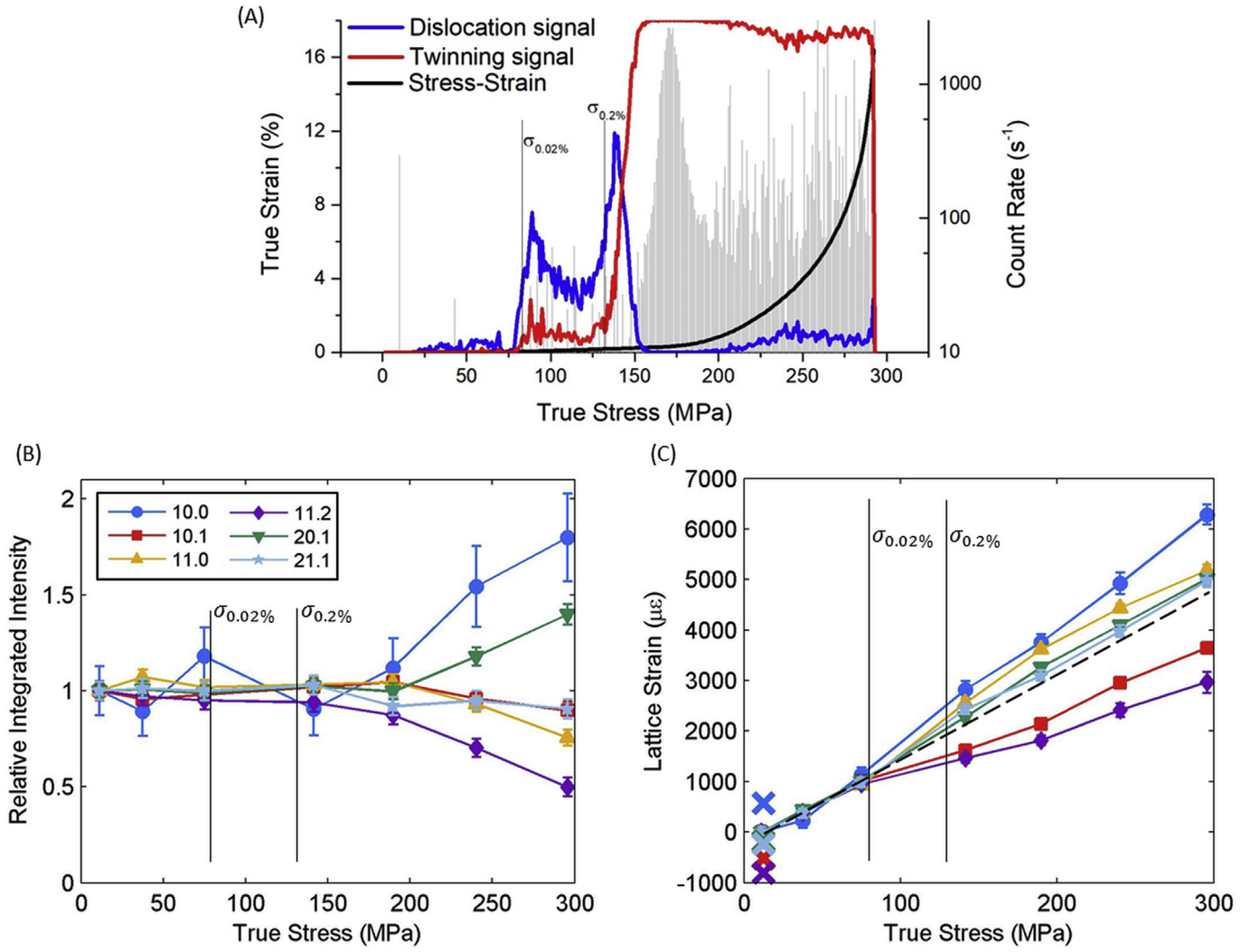

Fig. 4. (A) Acoustic emission results, (B) relative integrated intensity evolution, and (C) lattice strain evolution for a dogbone under tensile load (crosses mark the lattice strains after unload).

Table 2
NRSS values for the dogbone test.

Def. mode	{10.1}	{20.1}	{10.0}	{21.1}	{11.0}	{11.2}
Ba⟨*a*⟩	0.360	0.216	0	0.190	0	0.446
Pri⟨*a*⟩	0.337	0.404	0.433	0.476	0.433	0.314
Pyr⟨*a*⟩	0.467	0.458	0.382	0.479	0.382	0.382
$Pyr^{2nd}\langle c+a\rangle$	0.324	0.380	0.335	0.482	0.446	0.402
TTW	0.027	0	0	0.005	0	0.137

related to twinning, but it is unlikely because the grain family has an NRSS = 0 for TTW. Additionally, the acoustic emission registers no twinning signal in this regime. Therefore the intensity variations are more likely due to poor counting statistics.

Between 75 and 140 MPa, the AE dislocation signal suddenly increases and the lattice strains diverge. This stress range corresponds to a microplastic regime dominated by dislocation generation. The {10.1} and {11.2} grain families shed load well below macroscopic yield, implying that these families are already undergoing plastic deformation. These families have a high NRSS for *Ba*⟨*a*⟩ slip, the slip system with the lowest CRSS (Table 1), and are thus plastically softer than the surrounding grains. The load they shed is redistributed to the plastically harder grain families. Due to the strong basal texture, these soft grain families represent only a small fraction of the total grains in the dogbone. This explains why the onset of plasticity in these grains is not visible in the macroscopic mechanical response.

Just after 0.2% yield (132 MPa), there is a sudden increase in the AE count rate and twinning signal (Fig. 4A). The energy released by a single twinning event is much higher than that of a single dislocation moving. Thus, although Fig. 4A shows that the twinning plays a large role in this plastic regime, dislocation-based deformation is still active—the signal is just dwarfed by the twinning signal. At this point, the integrated intensity of the {10.0} grain family increases significantly, while the {11.2} intensity decreases significantly (Fig. 4B). The particularly strong decrease in {11.2} and simultaneous increase in {10.0} reflection intensities can be attributed to $\{10\bar{1}2\}$-type TTW, also observed in Ref. [16]. Although the NRSS for TTW of the {11.2} grain family is low (NRSS = 0.137), it is the highest NRSS for grain orientations that we measure that are present in the initial texture. The newly-oriented {10.0} twins have NRSS = 0 for basal slip and so they are expected to become plastically harder with twinning, which is reflected in their increasing lattice strain (Fig. 4C).

With further plastic deformation (>200 MPa) the AE dislocation

signal becomes stronger and the integrated intensity of the {20.1} grain family increases while the intensity of {11.0} grain family decreases. Simultaneously, the {11.0} grain family appears to shed load while the {10.1} and {11.2} grain families take more load again. The approximately linear evolution of the {20.1} lattice strain suggests that the intensity increases of the grain family are related to twinning. The parent grains related to TTW for this family are in the $\{4\bar{1}.4\}$ grain family, which diffracts out of range of our detector. The NRSS is 0.107 for this grain family, which is higher than all of the measured grain families except for {11.2}.

NRSS analysis suggests that the moderate intensity drop of the {11.0} grain family, on the other hand, is due to dislocation-related grain rotation. The load-shedding of the {11.0} grain family suggests the activation of $Pyr^{2nd}\langle c+a\rangle$ slip in these grains because pyramidal slip is the only deformation mode for which the {11.0} family has a higher NRSS than {10.0} family, which does not shed load. This was also observed by Muránsky et al. [16]. The activation of $\langle c+a\rangle$ slip directly implies that $Pri\langle a\rangle$ slip is already active, because the two deformation modes have similar NRSSs but $Pri\langle a\rangle$ slip has a lower CRSS for uniaxial loading (Table 1). Thus the dogbone deformation must initially be dominated by $Ba\langle a\rangle$ and simultaneous TTW, with $Pri\langle a\rangle$ and then $Pyr^{2nd}\langle c+a\rangle$ slip at later stages of deformation.

3.2. Multiaxial monotonic loading (cruciform)

Fig. 5 displays the mechanical response for the three monotonic load paths that have been performed. The applied forces are plotted against the plastic component of the von Mises strain. Due to the ring effect, the force ratios of the 1:0 and 7:10 monotonic loads do not correspond to the same strain ratios. The measured strain ratios are shown below. Because of the complex shape of the cruciform it is not possible to directly convert applied force in the arms into stress at the gauge volume. Therefore these force-accumulated plastic strain curves cannot be directly compared with one another.

3.3. Neutron diffraction and EBSD analysis

Fig. 6 displays the peak evolution for 1:0, 1:1, and 7:10 monotonic loading of the cruciform-shaped samples. The relative integrated intensity is shown as a function of the equivalent strain for each loading mode (Fig. 6A,C,E), and the corresponding lattice strain is shown as a function of the force on axis 1 (Fig. 6B,D,F). The integrated intensity of each peak is normalized by dividing by the initial value. In the lattice strain evolutions, the crosses show the lattice strain in the unloaded state due to residual stresses. The lower magnitude of the residual lattice strains for the 1:1 and 7:10 loads is due to the increasing Poisson contraction on axis 1 caused by the increasing relative strain component on the transverse axis [48]. NRSS grain distributions for the 1:0 and 1:1 monotonic loads are shown in Fig. 7. The NRSS distribution for 7:10 monotonic loading is available online as supplementary material.

Fig. 8 shows the EBSD analysis for the 1:0 (Fig. 8A–C) and 1:1 (Fig. 8D–F) monotonic loads. The IPF maps are shown on the left, the grain boundary maps with highlighted twin boundaries in the middle, and pole figures on the right. EBSD images for the 7:10 monotonic load are not shown because its behavior was similar to the 1:1 load. Note: the EBSD sample for the 1:0 montonic load is *not* the same sample that was tested *in situ*. The sample was deformed *ex situ* to an equivalent strain of 4.88%. Thus, the microstructure in Fig. 8A–C is representative of the starting microstructure for all of the LPC reloads.

During the 1:0 monotonic load, the evolution of the integrated intensity is very similar to that of the dogbone, despite the presence of the ring effect. TTW from the {11.2} grain family into the {10.0} family results in a decrease in intensity of the former and an increase in the latter (Fig. 6A). This twinning system is seen in the IPF map (Fig. 8A) as yellow-green parent grains with blue twins and appears as the presence of intensity around the TD poles of the pole figure (Fig. 8C). The IPF map also shows several grains with dark purple twins which contribute to the intensity increase of the {20.1} grain family (green curve, Fig. 6A). Different twinning systems are visible in several other grain orientations. These grain orientations, however, are diffracting outside of the angular range of the detector and are therefore not seen in the neutron diffraction pattern.

Despite the similarities of the intensity evolution with the dogbone sample, the ring effect has a noticeable influence on the lattice strains of the measured grain families (Fig. 6B). The {10.1} and {11.2} grain families are the most plastically soft for low-CRSS $Ba\langle a\rangle$ slip (Fig. 7A) and they plastify early in the microplastic regime (Fig. 6A). The {20.1} and {21.1} families plastify at higher stresses, which causes the relaxation in the lattice strain at 9 kN. The plasticity is likely due to $Ba\langle a\rangle$ slip, as the NRSS distributions for {21.1} and {20.1} have lower values than those of the {10.1} and {11.2}

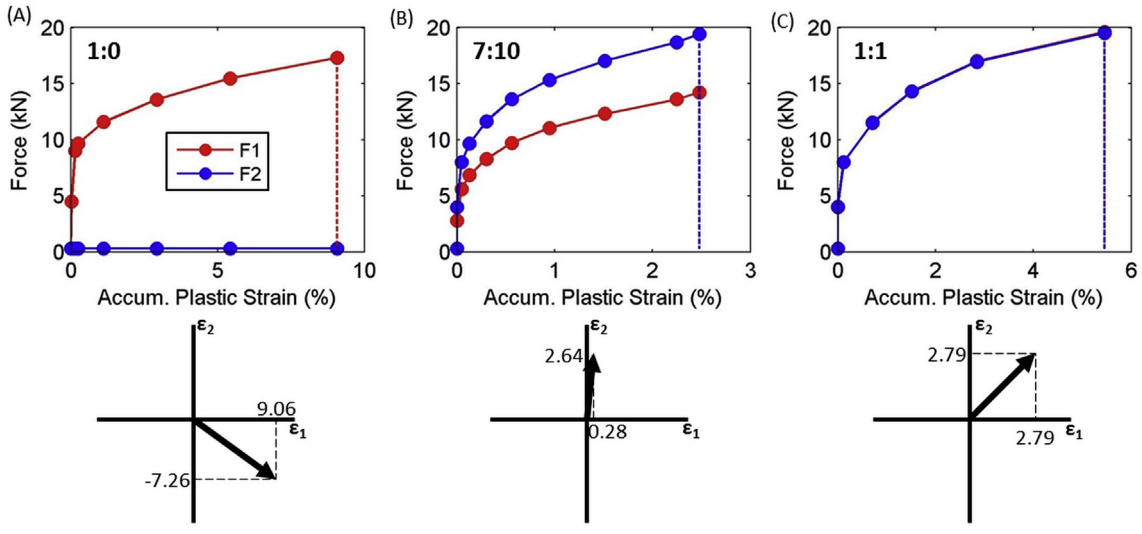

Fig. 5. Force-accumulated plastic strain plots for the (A) 1:0, (B) 7:10, and (C) 1:1 monotonic loads. The corresponding strain paths are shown below each load path.

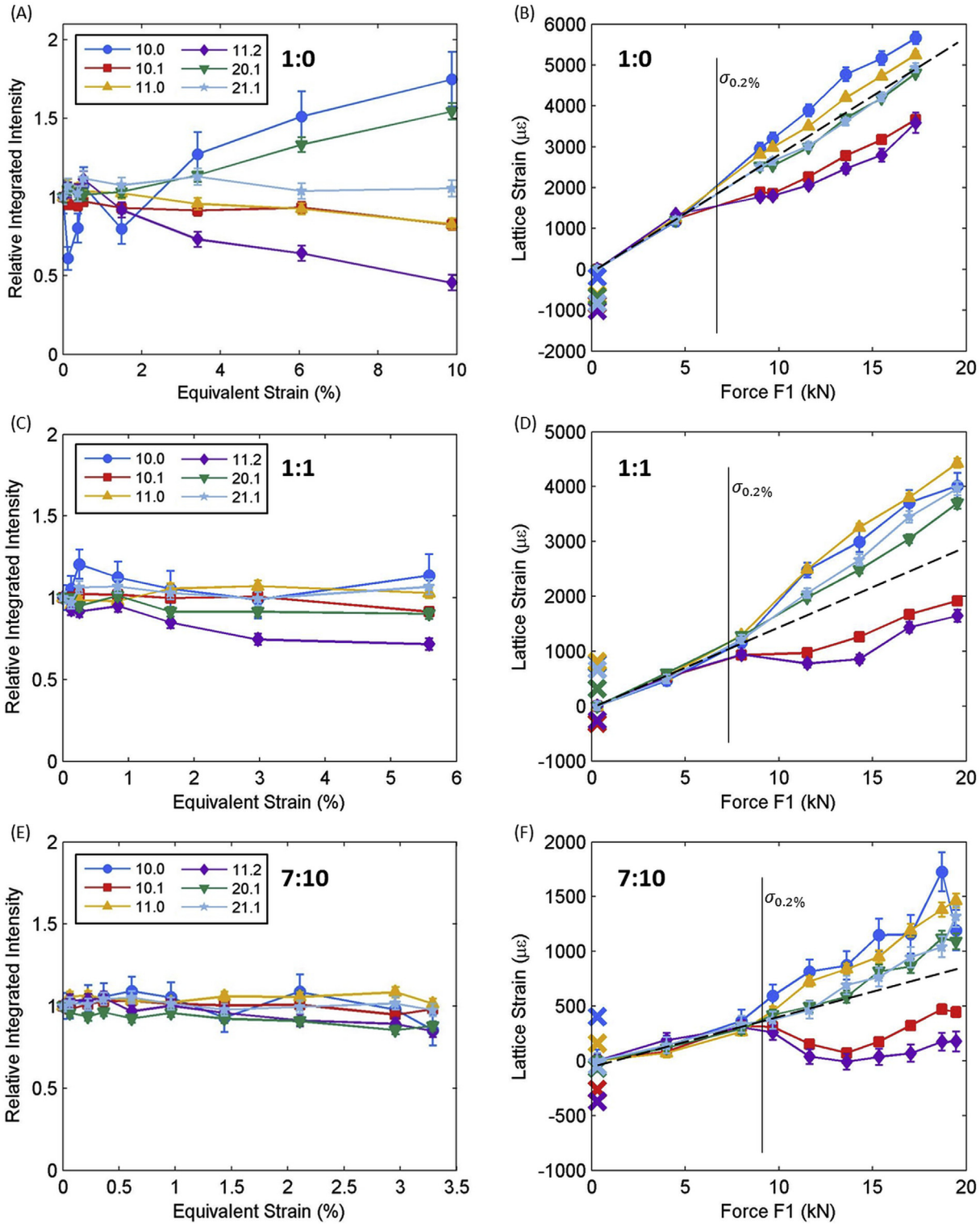

Fig. 6. Integrated intensity and lattice strain evolution from *in situ* neutron diffraction of cruciforms during (A,B) 1:0, (C,D) 1:1, and (E,F) 7:10 monotonic loads.

(Fig. 7A). One could argue that *Pri*⟨*a*⟩ or *Pyr*⟨*a*⟩ slip could be responsible for the load shedding, but the NRSS distributions are similar for all diffraction peaks so load shedding should then be observed in all families if that were the case. The {10.0} and {11.0} families are poorly oriented for *Ba*⟨*a*⟩ slip and thus remain plastically hard. It is likely that *Pri*⟨*a*⟩ or *Pyr*⟨*a*⟩ slip are activated in these grains around the same time as *Ba*⟨*a*⟩ slip, because the NRSS values for *Pri*⟨*a*⟩ or *Pyr*⟨*a*⟩ slip are 3–4 times larger than *Ba*⟨*a*⟩ slip, enough to counter the differences in CRSS. Dislocation-based grain rotation for these grain families is seen as a "smearing" of the basal texture in the pole figure (Fig. 8C). After unloading, the ring effect results in a compressive residual stress in the unloaded state that pushes all of the measured grain families into compression (marked "x" in Fig. 6B).

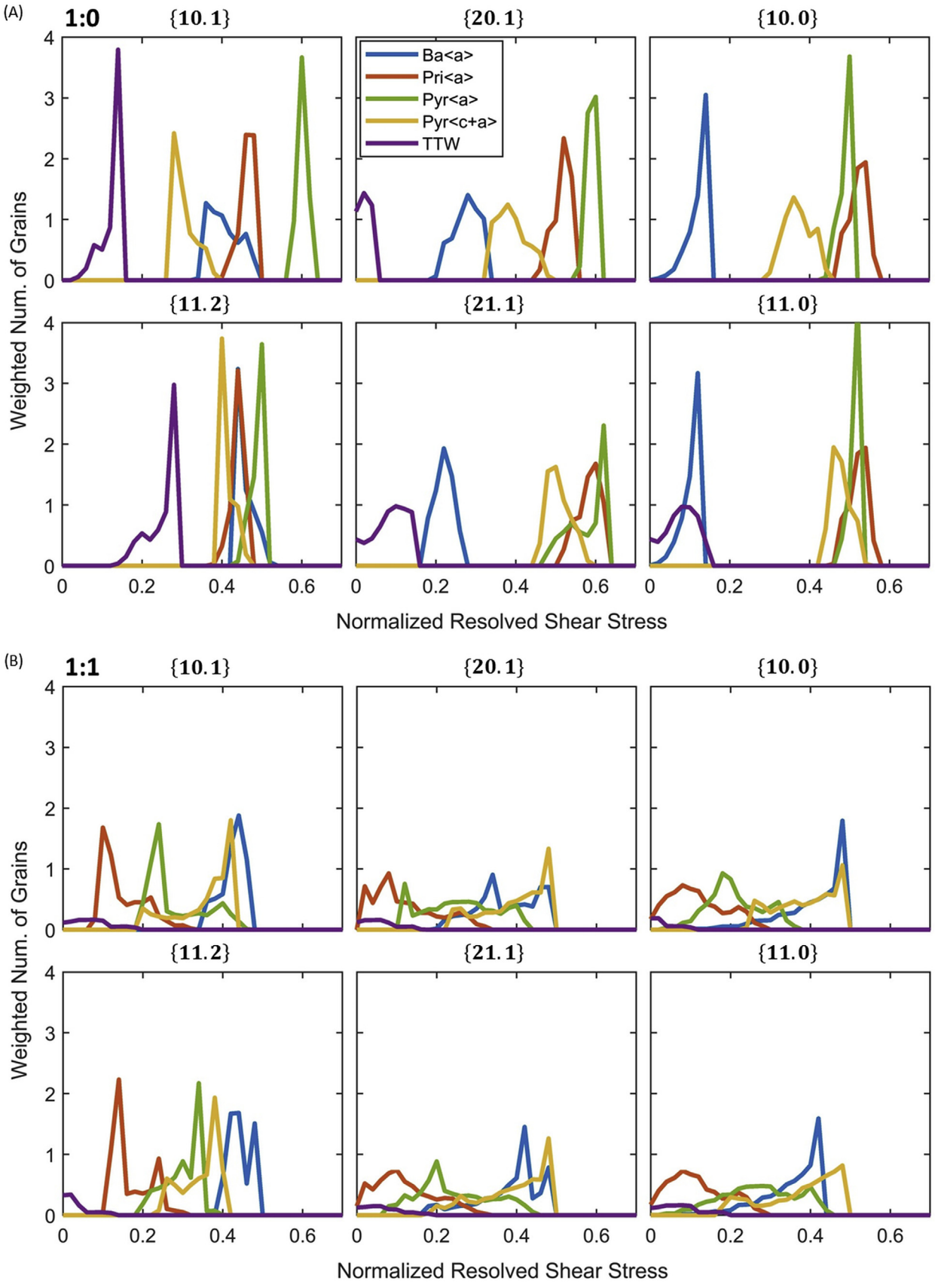

Fig. 7. NRSS distributions for the 1:0 and 1:1 monotonic loads.

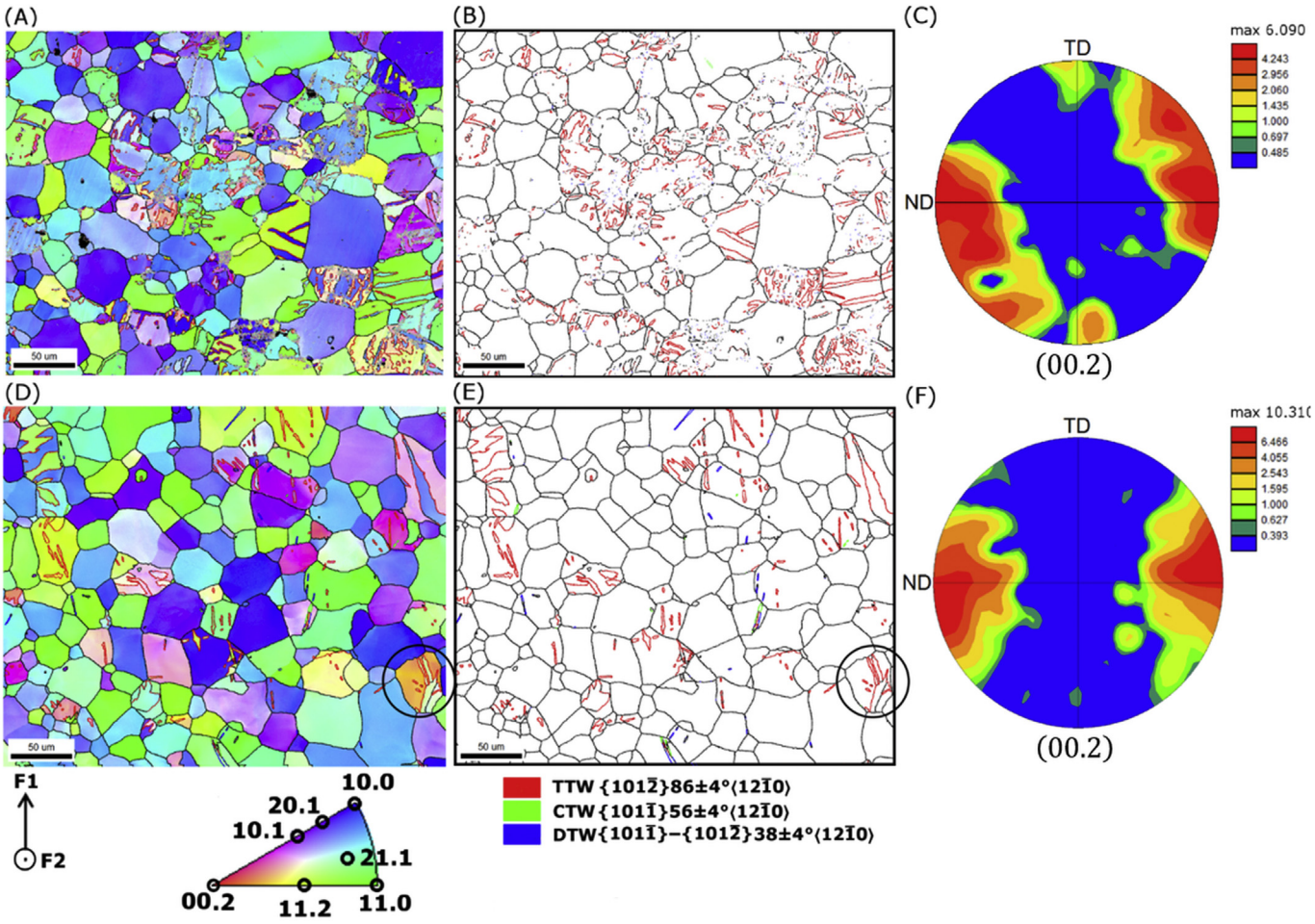

Fig. 8. Post-mortem IPF map, grain boundary map with highlighted twin boundaries, and (00.2) pole figure for the (A,B,C) 1:0 monotonic load and (D,E,F) 1:1 monotonic load.

During the 1:1 monotonic load, the intensities are relatively stable (Fig. 6C). This suggests that the role of twinning is minimal, at least for $\varepsilon_{Eq} < 5.5\%$. A small amount of TTW and $\{10\bar{1}1\} - \{10\bar{1}2\}$ double twinning is observed in the IPF maps (Fig. 8D,E). The pole figure in Fig. 8F shows a slightly stronger basal texture than the initial microstructure, and the {11.2} - {10.0} twinning system is not activated in this load path, evident from the lack of intensity at the TD poles of the pole figure (Fig. 8F). There is, however, still a gradual decrease in integrated intensity of the {11.2} peak (Fig. 6C). The intensity change is likely due primarily to grain rotation from dislocation activity because there are only a few {11.2} grains that are capable of twinning. Note, however, that the IPF map (Fig. 8D) shows that there are some narrow tension twins in a few {11.2} grains which also contribute to the intensity decrease.

The NRSS values for TTW were calculated for several twinned grains in the 1:1 load. One such grain is shown in Fig. 9. The selected variants V6 and V5 have NRSS values of 0.155 and 0.073, respectively, the first and third highest NRSS values (Fig. 9D). V3, which has the second highest NRSS value (0.099) is not observed. Non-Schmid twinning and twin variant selection has been previously observed in AZ31 [49,50] and is discussed further in Section 4. In many twinned grains it appears that nucleation is preferred to growth of existing twins.

For 1:1 biaxial loading, NRSS analysis shows that all grain families have grains well-oriented for low-CRSS $Ba\langle a\rangle$ slip. However, the {10.1} and {11.2} grain families have nearly all grains with high NRSS, whereas the other families have a much wider distribution. The {10.1} and {11.2} grain families plastify early in the microplastic regime as $Ba\langle a\rangle$ slip is activated in a majority of the grains (Fig. 6D). It is likely that the grains with high NRSS values in the other families plastify early as well, but the response measured by diffraction averaged out with the harder grains and the family as a whole takes more load. As the {10.1} and {11.2} grain families harden, load is redistributed to the other grain families, resulting in the load shedding that is seen in the {10.0} and {11.0} grain families at F1 = 11.5 kN.

From the lattice strain evolution (Fig. 6D), the {10.0} and {11.0} grain families seem to take always more load. The {11.0} family does not have any grains with NRSS >0.44 and is therefore indeed plastically hard compared to the other grain families. The {10.0} family, however, has many grains with high NRSS values for $Ba\langle a\rangle$ slip which are plastically soft. Load shedding is not observed because {10.0} grains are oriented such that one *Baa* slip system with a burgers vector perpendicular to the diffraction vector **Q** is significantly preferred over the other two. Thus, the {10.0} family is plastically soft in some directions perpendicular to **Q**, but hard along **Q**. The other five grain families in this study deform along several slip systems, so the lattice strain evolution can be interpreted as a result of plasticity.

During the 7:10 monotonic load, the intensities are very stable for $\varepsilon_{Eq,\ 7:10} < 3.5\%$ (Fig. 6E) and the lattice strain behaviors generally follow the same trends as in the 1:1 load (Fig. 6F). It is expected that the deformation behavior is dominated by $Ba\langle a\rangle$ slip with reduced twinning, as observed for the 1:1 load.

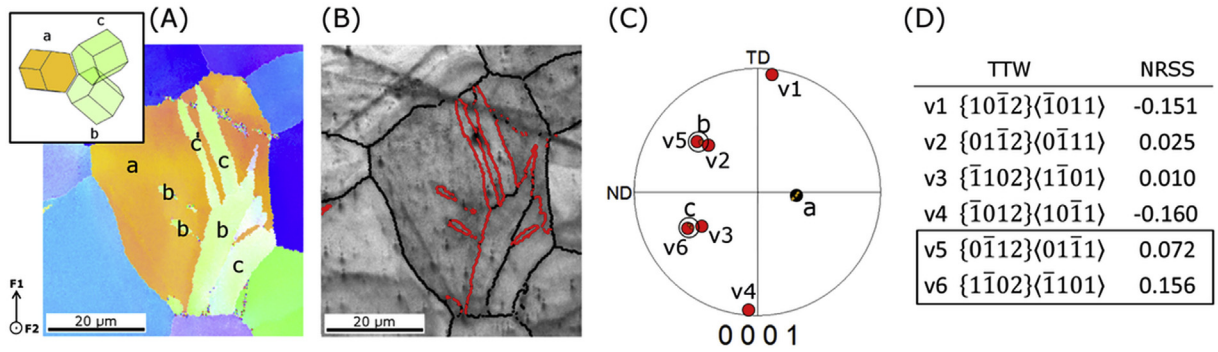

TTW	NRSS
v1 $\{10\bar{1}2\}\langle\bar{1}011\rangle$	-0.151
v2 $\{01\bar{1}2\}\langle0\bar{1}11\rangle$	0.025
v3 $\{\bar{1}102\}\langle1\bar{1}01\rangle$	0.010
v4 $\{\bar{1}012\}\langle10\bar{1}1\rangle$	-0.160
v5 $\{0\bar{1}12\}\langle01\bar{1}1\rangle$	0.072
v6 $\{1\bar{1}02\}\langle\bar{1}101\rangle$	0.156

Fig. 9. (A) IPF map and (B) grain boundary map of a twinned grain after the 1:1 monotonic load. (C) Pole figure with the orientations of the parent grain and six $\{10\bar{1}2\}$ twin variants. (D) Calculated NRSS values for the six twin variants.

3.4. Load path changes (cruciform)

During the LPC experiments the cruciform samples are first preloaded uniaxially (force ratio 1:0) along the rolling direction to a total plastic strain of 3.7–4.7%. After the applied force is released a second load is applied, with load ratios of 0:1, 7:10 and 1:1 as described in Fig. 2. Due to the ring effect, the strain path change angle is not the same as the angle between the applied loads. This is shown in Fig. 10 for the three LPCs. The angles between the directions of the plastic strain during the strain path change are 170°, 135° and 90° for the 0:1, 7:10, and 1:1 LPCs, respectively, as calculated from the macroscopic strain measurements.

The mechanical response of the LPCs is shown in Fig. 10, with the corresponding strain path change shown below each LPC. As with the monotonic multiaxial loads, it is not possible to directly compute the stress state in the center of the cruciform from the force in the arms, so applied force is shown instead. The slight variations in prestrain were caused by differences in the thickness of the samples due to machining tolerances. However, the observed diffraction data suggests that the microstructure evolution during prestrain was very similar for each sample. In both the 7:10 and 1:1 reloads, there is a significant overshoot in force-accumulated plastic strain curve, whereas in the 0:1 reload there is an undershoot. This suggests a higher yield stress for the 7:10 and 1:1 LPCs and a lower yield stress in the 0:1 LPC upon reloading.

3.5. Neutron diffraction and EBSD analysis

Fig. 11 shows the diffraction peak evolution for the 0:1, 7:10, and 1:1 LPCs. The two vertical lines on the integrated intensity graphs show where the load path changed: the left line indicates the end of the preload, the right the beginning of the second load, and in between the unload. During the preload, the peaks behave as expected from the 1:0 monotonic load test (Fig. 6A). Equivalent strain was used instead of accumulated plastic strain to capture the behavior during the unload. The magnitudes of the integrated intensity changes are lower because the samples are only strained to 3.7–4.7%. In the 0:1 LPC, the (00.2) intensity is normalized with respect to the final value because the peak is not visible in the preload due to the texture. Due to the cruciform geometry, it was only possible to achieve 2% and 1.2% equivalent strain in the gauge section for the reloads of the 1:1 and 7:10 LPCs, respectively.

Fig. 13 shows the EBSD analysis for the 0:1 LPC (Fig. 13A–C) and 1:1 LPC (Fig. 13D–F). The IPF maps are shown on the left, the grain boundary maps with highlighted twin boundaries in the middle, and pole figures on the right. EBSD images for the 7:10 LPC are not shown because its behavior was similar to the 1:1 LPC.

During the reload of the 0:1 LPC, the lattice strain differs considerably between the first and second measurement points. This apparent "anisotropy" in the elastic strain behavior must be ascribed to very early microplastic deformation during the reload. It

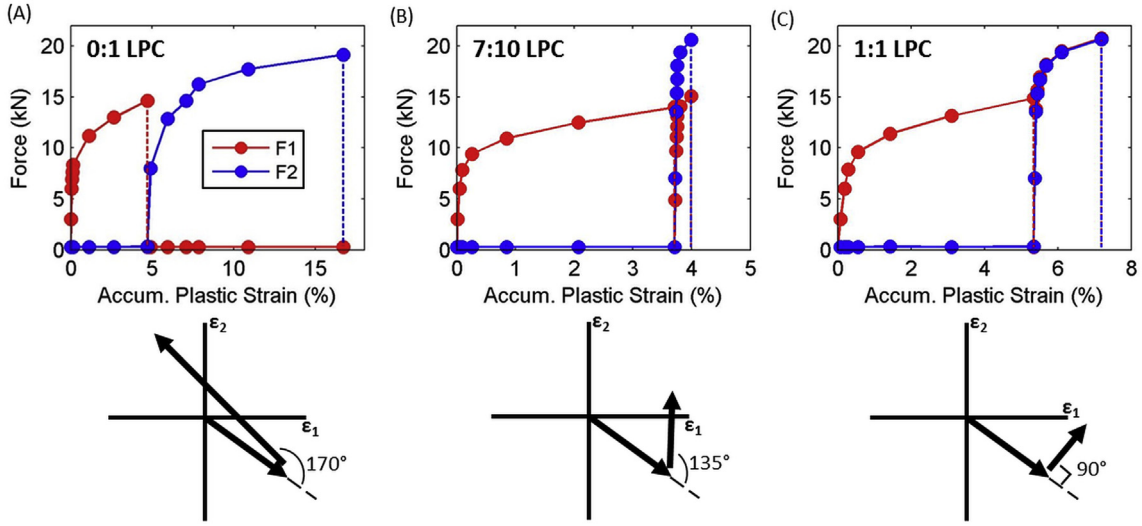

Fig. 10. Force-accumulated plastic strain plots for the (A) 0:1, (B) 7:10, and (C) 1:1 load path changes. The corresponding strain path changes are shown below each load path.

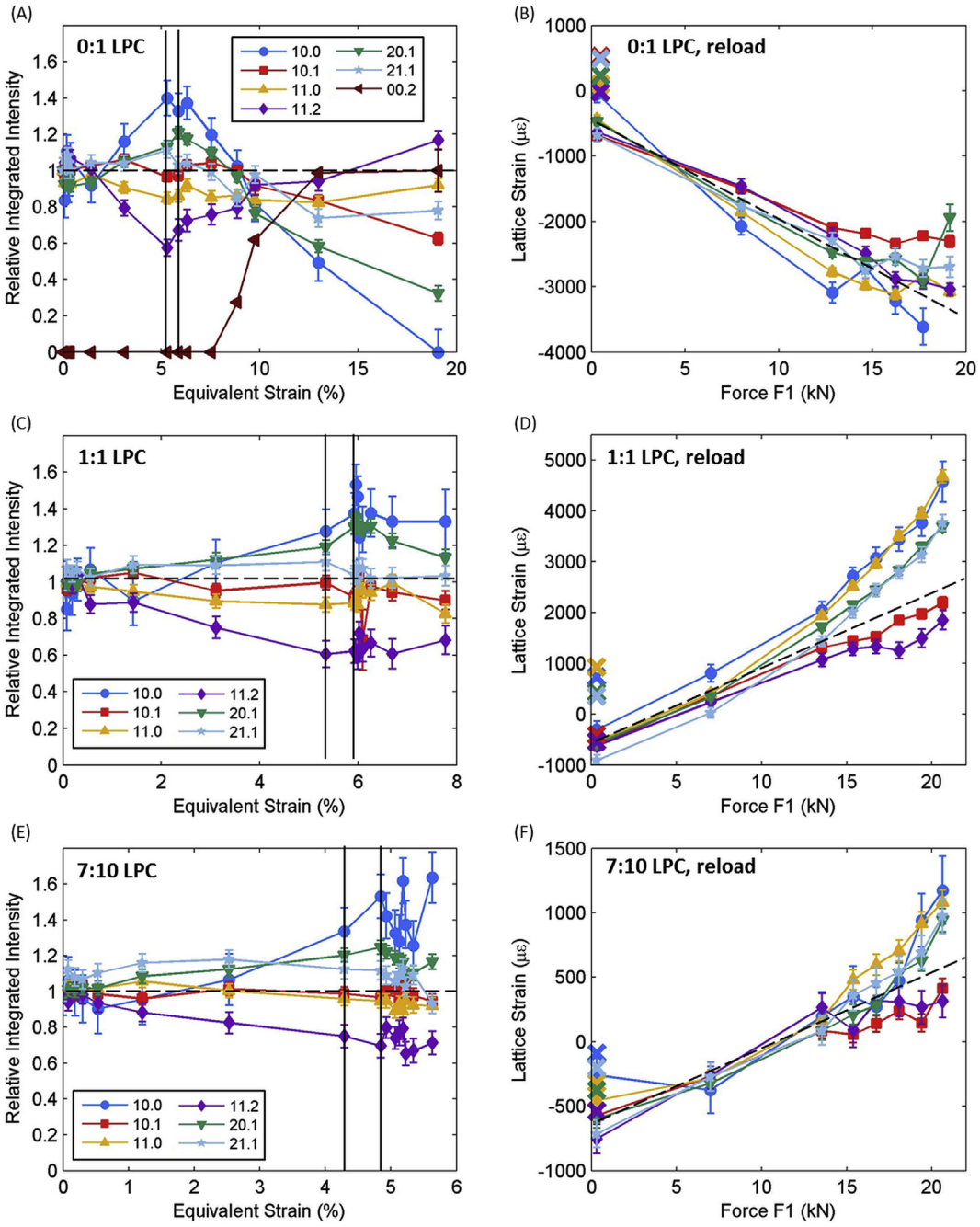

Fig. 11. Integrated intensity and lattice strain evolution from *in situ* neutron diffraction of cruciforms during (A,B) 0:1, (C,D) 1:1, and (E,F) 7:10 LPCs. Black vertical lines on the integrated intensity plots demarcate the unload: to the left is the 1:0 preload, in between is the unload, and to the right is the reload. Lattice strains are shown only for the reload. NRSS grain distributions for the 0:1 and 1:1 LPCs are shown in Fig. 12. The NRSS distribution for 7:10 LPC is available online.

is also evident in the mechanical response in Fig. 10, which already shows a slight increase in plastic strain between the unloaded state and the first point of the reload. In this microplastic regime, the plastically soft {10.1} and {11.2} grain families are already shedding load. It is anticipated that if an intermediate measurement point was taken, the lattice strain behavior would be isotropic in the elastic regime and then deviate at the onset of microplastic yield.

As the sample plastifies, the integrated intensity of the {10.0} grain family decreases while the {11.2} and (00.2) grain family intensities increase significantly (Fig. 11A). These behaviors are a result of primary twinning combined with de-twinning and secondary twinning. During the preload, TTW of {11.2} grains create twins in the {10.0} orientation. During the 0:1 reload the {10.0} grain family, including the twins, are oriented well for TTW into the (00.2) orientation. This results in de-twinning back into the {11.2} orientation and secondary TTW into the (00.2) orientation. The extensive twinning into the (00.2) orientation is seen in the IPF map in Fig. 13A. The blue parent grains with red twins are the {10.0} - (00.2) TTW system. Several of the grains have been completely swallowed up by the (00.2) twins.

For the last 7% of strain, the integrated intensity of the (00.2) grain family stays constant, suggesting that twinning into this orientation has mostly stopped. However, the integrated intensity

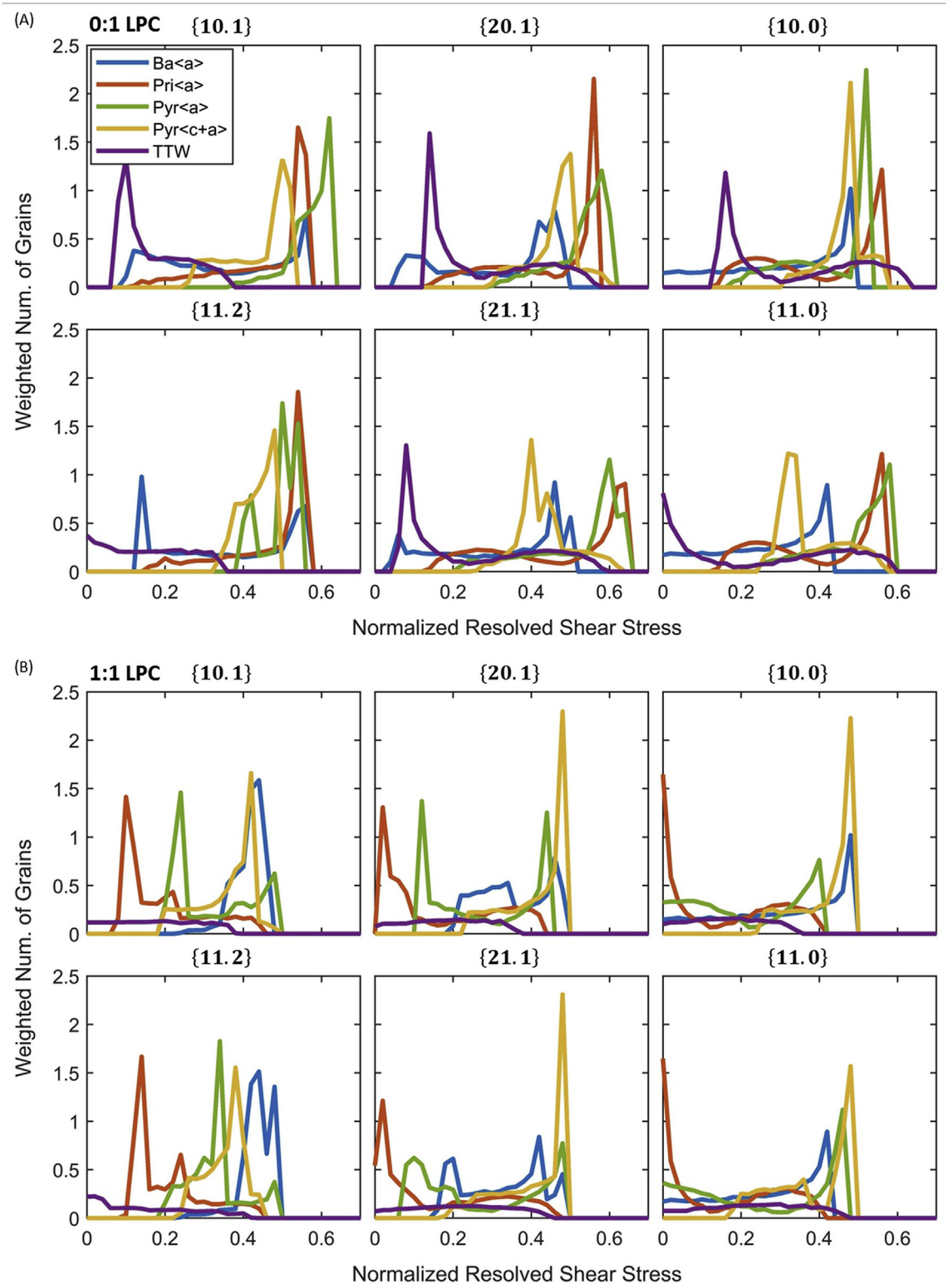

Fig. 12. NRSS distributions for the reloads of the 0:1 and 1:1 LPCs.

of the {10.0} grain family continues to decrease until almost no grains remain in diffraction condition. This is due to twinning of {10.0} grains into orientations *near* the (00.2) peak but just outside of the ±2.5° detector tolerance. In this strain range, the integrated intensity of the {11.2} family increases past the initial intensity. No twinning is observed into the orientation (Fig. 13A,C) and the intensity changes gradually compared to the twinning families, so it is likely that the intensity changes are due to grain rotation from dislocation activity.

The {10.1}, {20.1}, and {21.1} grain families also show a decrease in integrated intensity in the plastic regime (Fig. 11A). A large fraction of the grains in the {21.1} and {20.1} families are

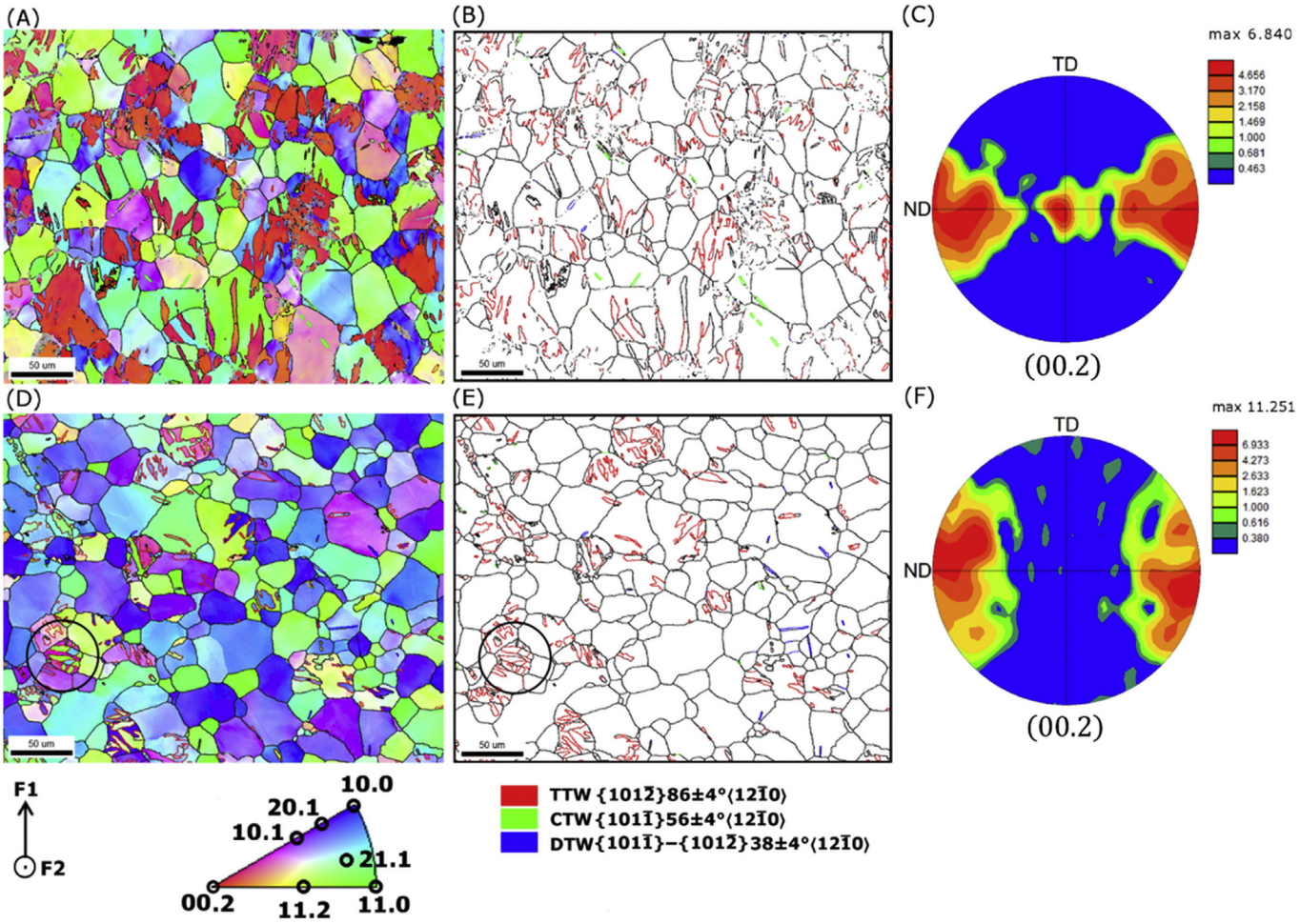

Fig. 13. Post-mortem IPF map, grain boundary map with highlighted twin boundaries, and (00.2) pole figure for the (A,B,C) 0:1 LPC and (D,E,F) 1:1 LPC.

well-oriented for TTW, with NRSS values greater than 0.4. TTW is visible in the IPF map (Fig. 13A) in both the green {21.1} and the dark purple {20.1} grains. The {10.1} grain family, on the other hand, has the majority of its grains with a low NRSS for TTW. Twinning is hardly active in these grains (Fig. 13A). Thus, the intensity drop is more likely related to dislocation-related grain rotation.

Both the {10.1} and {11.2} grain families shed load in the microplastic regime (Fig. 11B) because they are well-oriented for *Ba*⟨*a*⟩ slip. However, immediately after macroplastic yield, the {11.2} grain family begins to take more load while the {10.1}, {20.1}, and {21.1} families all shed load. As discussed previously, the {20.1} and {21.1} families have begun twinning and thus are able to accommodate strain with little hardening. The {10.1} family, however, is not twinning significantly. The only deformation mode for which the {11.2} family is harder than the {10.1} family is *Pyr*⟨*a*⟩ slip, implying that this mechanism may be active. The activity of this mechanism is often ignored in crystal plasticity models, but several studies have shown that the inclusion of this mechanism can improve predictions of the lattice strain evolution of various loading modes [9,16].

During the second load of the 1:1 LPC (Fig. 11C), the integrated intensities for all peaks stay relatively stable over $\varepsilon_{Eq} < 2\%$. This suggests that twinning activity is limited, and the twins from the preload are not de-twinning. The pole figure shows a strengthening of basal texture like the 1:1 monotonic load (Fig. 13F). As in the 1:1 monotonic load, some $\{10\bar{1}1\} - \{10\bar{1}2\}$ double twinning is observed in the IPF map (Fig. 13D,E). Yellow-green grains with blue tension twins are visible that are similar to those in the preload, confirming the absence of de-twinning. The presence of these twins from the preload causes intensities at the TD poles of the pole figure which are not obvious due to the high values at other orientations.

A few grains show very complex twinning after the 1:1 LPC. The twinning in the reload was dominated by the nucleation of new twins rather than the growth of existing ones. Fig. 14 examines the twin variant selection in one heavily-twinned grain (circled in Fig. 13D,E). The grain in Fig. 14A has three primary twin variants V_I1, V_I2, and V_I3, along with one secondary twin orientation, $V_{II}1$, which twinned from V_I1. The “h” and “j” twins (NRSS 0.369 and 0.255, respectively) are suspected to have formed during the 1:0 preload. However, it is possible that the “j” twins formed during the 1:1 reload, as they have a very high NRSS of 0.283. During the reload, the “i” twins form as secondary twins within the “h” primary twins. The “k” twin is then nucleated at the triple junction of the “h”, “j” and “i” twins. As in the 1:1 monotonic load, the selected variants do not necessarily correspond with the highest NRSS value, which is discussed in Section 4. This activation of multiple twin variants in one grain is not seen in any of the other LPCs.

The lattice strain evolution during the reload shows that the {10.1} and {11.2} grain families shed load early (Fig. 11D) as they have a large fraction of grains well-oriented for low-CRSS *Ba*⟨*a*⟩ slip.

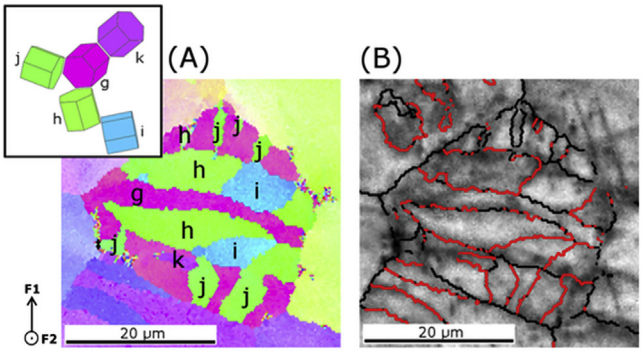

TTW	NRSS 1:0 (uniaxial)	1:1 (equibiaxial)$_I$	1:1 (equibiaxial)$_{II}$
v1	0.369	-0.083	0.455
v2	0.141	0.072	0.111
v3	0.255	0.283	0.067
v4	0.322	-0.065	0.425
v5	0.069	0.037	0.095
v6	0.231	0.231	0.081

Fig. 14. (A) IPF map and (B) grain boundary map of a heavily-twinned grain after the 1:1 LPC. (C) Pole figure with the orientations of the parent grain and six $\{10\bar{1}2\}$ twin variants. Variant twin plane and shear direction are the same as in Fig. 9 (D) Calculated NRSS values for the six twin variants.

However, they quickly harden and begin to take load again after very little strain. All grain families are plastically hard during the reload, despite having grains well-oriented for $Ba\langle a\rangle$ slip. This suggests that there is significant plastic hardening from dislocations generated during the preload in all grains.

During the second load of the 7:10 LPC, the integrated intensities also do not change significantly (Fig. 11E), suggesting there is no twinning activity (at least for $\varepsilon_{Eq} < 1.2\%$). The large intensity fluctuations of the {10.0} family are due to low counting statistics—such behavior over small strain ranges during a continuous load are not physical.

As in the 7:10 monotonic load, the {10.1} and {11.2} grain families shed load first while the {10.0} and {10.1} families take the most load (Fig. 11F). This behavior is expected from NRSS analysis (available online as supplementary material). Unfortunately, the sample reached such low strains that it is hard to draw further conclusions from the lattice strain evolution.

The effect of the preload is also seen in the behavior of the peak broadening. Fig. 15 shows the peak broadening of the {10.1} peak for the monotonic loads and LPC reloads. Monotonic loads are shown as dashed lines, and the corresponding LPC reloads are shown as solid lines of the same color. The peak broadening during deformation of the dogbone is shown in black. Only the {10.1} reflection is shown as the peak broadening in the other reflections shows the same trends. EBSD analysis shows that the average grain size does not change significantly, despite the observed twinning, so the peak broadening behavior is attributed to changes in dislocation density during the tests.

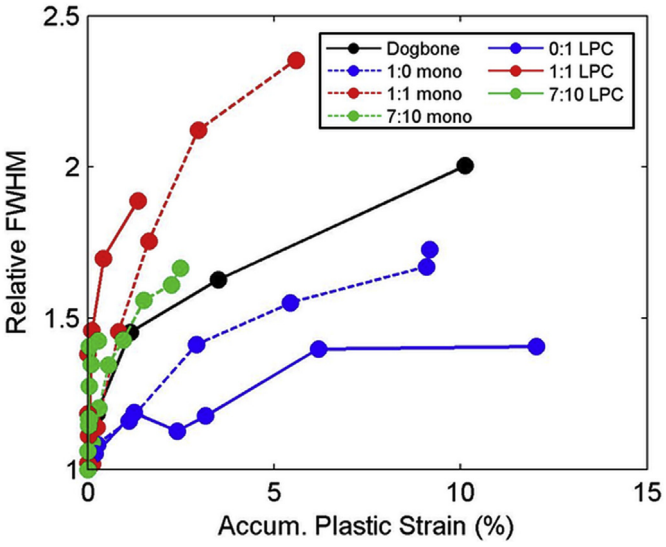

Fig. 15. Peak broadening of the {10.1} grain family. For the LPCs, only the reloads are shown.

The 1:0 monotonic load has lower peak broadening than the dogbone while the broadening of the 7:10 and 1:1 monotonic loads is increased. After a 1:0 preload, the 0:1 reload shows even lower peak broadening than the 1:0 load. The 7:10 and 1:1 reloads show increased broadening compared to the corresponding monotonic loads. Interpretations of these observations are discussed below.

4. Discussion

The combination of *in situ* neutron diffraction, acoustic emission, and EBSD is a powerful tool to identify active deformation mechanisms during multiaxial loading of AZ31. The interpretation of the diffraction data relies on NRSS analysis. Obviously, such an analysis has its limitations, because it does not take into account the effects of elastic and plastic anisotropy or texture evolution. However, since AZ31 is nearly elastically isotropic, NRSS analysis at the onset of plasticity can be justified. At later stages of deformation, plastic anisotropy becomes more important and the true behavior can only be captured by crystal plasticity models. In literature there exists large variations for the reported CRSS values of the various deformation mechanisms in AZ31 (see Table 1). It is anticipated that the findings of this study would be useful for the validation of improved crystal plasticity finite element (CPFE) models.

4.1. Monotonic loads

The results from the dogbone confirm the findings of crystal plasticity simulations of uniaxial tension [13,16,51]: at the onset of plasticity $Ba\langle a\rangle$ slip is activated in a subset of grains with their *c*-axis away from the sheet normal followed by TTW-induced plasticity and, later, $Pri\langle a\rangle$ slip. At larger plastic strains, $\langle c+a\rangle$ slip on {11.2} 2nd order pyramidal planes is activated, in agreement with the findings of Muránsky et al. [16]. AE measurements indicate no signs of twinning in the elastic regime (<75 MPa), despite large intensity variations in the {10.0} grain family. This finding is in contrast to the study of Muránsky, who proposed that the variations were due to tension twinning in a few well-oriented grains.

In the 1:0 monotonic load $Ba\langle a\rangle$ is again activated in the microplastic regime in the {10.1} and {11.2} grain families, followed by TTW, then $Pri\langle a\rangle$ and $Pyr^{2nd}\langle c+a\rangle$ slip. The separation between the NRSS values for $Ba\langle a\rangle$ slip implies that grain families will begin to plastify one after another. The compressive transverse stress effectively improves the orientation of all measured grain

families for slip and TTW as compared to the dogbone.

The lower peak broadening observed in the cruciform versus the dogbone is a direct result of the ring effect. It has been shown that the out-of-plane texture is favourable for TTW when subjected to in-plane compression [5,20,29,32,52]. This is evident from the higher NRSS values for TTW in the cruciform for every grain family except the {10.0}. The additional compressive stress of the ring effect activates more TTW in the cruciform than in the dogbone, so fewer dislocations are needed to accommodate strain, explaining the lower peak broadening observed in the cruciform.

In the 1:1 monotonic load, every grain family observed in this study has grains which are well-oriented for low-CRSS $Ba\langle a\rangle$ slip (Fig. 7B). $Pri\langle a\rangle$ slip is likely limited under this stress state, as few grains have values of NRSS >0.2 for the mechanism. Conversely, $Pyr^{2nd}\langle c+a\rangle$ is promoted for this loading mode (Fig. 7B). Considering CRSS values reported by Ma [15], Wang [14,53], Hama [40], and Agnew [9], the NRSS distribution implies that in many grains $Pyr^{2nd}\langle c+a\rangle$ slip may be activated before $Pri\langle a\rangle$ slip. NRSS analysis also predicts that there should be very few grains that can twin, which is confirmed in both the integrated intensity evolution and EBSD results. Thus, $Pyr^{2nd}\langle c+a\rangle$ slip becomes particularly important as a way of accommodating through-thickness reduction.

VPSC modeling of 1:1 loading by Steglich et al. [35] support this idea, suggesting that 1) $Pyr^{2nd}\langle c+a\rangle$ slip is the dominant non-basal slip mechanism and 2) both twinning and $Pri\langle a\rangle$ slip are suppressed. However, their model suggests $CRSS_{Pyr^{2nd}c+a} < CRSS_{Pria}$, which is different than most literature (Table 1). Our analysis suggests that $Pri\langle a\rangle$ slip is still likely, just reduced compared to uniaxial loading. On the other hand, TEM observations by Chino et al. [34] show hardly any dislocations with a *c*-axis component over a nominal biaxial strain of 20%. However, they also saw more twinning, particularly contraction twinning, which could accommodate through-thickness strain in lieu of $Pyr^{2nd}\langle c+a\rangle$ slip. The stronger basal texture of the AZ31 used by Chino can account for these differences, as it should simultaneously lower the NRSS for $Ba\langle a\rangle$ slip and increase the NRSS values for contraction twinning.

Despite the basal texture, twin nucleation and growth is observed in several grains (Figs. 8 and 9). As also seen in Ref. [34], $\{10\bar{1}2\}$ TTW is the predominant twin mechanism, but double twinning is also present which can accommodate strain in the through-thickness direction. NRSS analysis of the twinned grains shows that the selected twin variants do not necessarily correspond to the highest NRSSs. One example is shown in Fig. 9. The selected variants have the first and third highest NRSS values. Non-Schmid twin variant selection has been previously described in Mg alloys as a result of short-range internal stresses at localized strain inhomogeneities between the parent grain and neighboring grains [49,50,54,55].

A 7:10 monotonic load showed similar behavior to the 1:1 load and the NRSS distributions are very similar for the grain families examined in this study. This suggests that applying a tensile load that opposes in-plane can limit twinning and promote slip. This can be understood by considering that extension twinning is a volume-conserving process—to accommodate extension along the *c*-axis, the grains must contract perpendicular to the *c*-axis. Hama et al. [40]. have previously suggested that the Poisson contraction in the transverse direction is important for twinning in a dogbone with a strong basal texture. Further tests at various load ratios should be performed to strengthen this assumption.

4.2. Load path changes

During the preload of the LPCs, both twinning and dislocations are generated. The mechanical response of the reload depends strongly on the angle of the LPC.

The reload of the 0:1 LPC shows a significant undershoot in the force-strain curve. This is suspected to be related to three mechanisms: 1) backwards motion of existing dislocations due to the Bauschinger effect, 2) de-twinning, and 3) primary and secondary TTW in the reload. All three mechanisms accommodate strain without increasing the dislocation density, which explains why the peak broadening is the lowest in this load path.

The 0:1 LPC corresponds to a 170° strain path change, nearly a reverse loading. Dislocations formed during the preload glide easily in the reverse direction aided by back stresses built up during the preload, i.e. the Bauschinger effect. The load reversal also promotes de-twinning, which is active almost immediately after loading begins. This is evident from the intensity changes in the {11.2} - {10.0} twin system. De-twinning is active before the appearance of the (00.2) peak, which implies that de-twinning has a lower CRSS than TTW. Reverse loading experiments performed on ZK60A [56] and AZ31 [32,57,58] have suggested that de-twinning has a lower CRSS than twinning as 1) there is no need for nucleation and 2) localized back-stresses formed between the twin and the matrix can be supportive. This can explain why some of the {10.0} twins de-twin rather than secondary twin, despite many grains having high NRSS values for TTW (Fig. 12). As the de-twinning mechanism is exhausted, basal slip initially dominates and non-basal slip increases as strain increases. This was also observed by Lou et al. [32]. and Wu et al. [58].

In addition to de-twinning, there are many {10.0} and near-{10.0} grains well-oriented for primary and secondary TTW into the (00.2) orientation. In all twinned grains, one- or two-variant TTW is observed, and the twin variants with the highest NRSS are activated. In grains with two variants, both produce strain along the same direction. It is clear from the IPF map (Fig. 13A) that twin growth is preferred to nucleation, as many of the twins have nearly consumed the {10.0} parent grains. This is typical of metals with high plastic anisotropy [59]. Twin transmission is seen across a few grains, but growth and intersection of existing twins was responsible for the majority of the twinning activity. Twin thickening is associated with low work hardening [60,61].

The growth of these twins causes a significant texture change, which is evident from the pole figure (Fig. 13C). The (00.2) orientation is poorly oriented for both $Ba\langle a\rangle$ and $Pri\langle a\rangle$ slip, so these grains become plastically hard. However, even after high NRSS TTW in the {10.0} grains is exhausted, twin nucleation and growth is observed in other grain families and the textural hardening seems to have little effect on the bulk mechanical response over the observed strain.

Both the 7:10 and 1:1 LPCs show a significant overshoot in the force-strain curve upon reloading. No significant twinning is observed except in a few grains, which show multivariant secondary twinning. The lack of low-CRSS twinning and hardening due to dislocations from the preload result in a rapid increase in dislocation density and thus the rapid peak broadening compared to the corresponding monotonic loads.

The results of the 1:1 LPC show that the basal texture is broken during the preload, but returns to a strengthened basal texture during the reload. The deformation primarily occurs by $Ba\langle a\rangle$ slip and twinning is limited to a few grains, which suggests that $Pyr^{2nd}\langle c+a\rangle$ slip is active early in the deformation. Unlike the initial texture, the prestrained texture has a significant number of grains with high NRSS for $Pri\langle a\rangle$ slip, which is expected to be more active than in the 1:1 monotonic load. These findings generally match the results of 90° strain path changes performed by two-step loading of cut dogbones [39,40]. Both groups found that the experimental yield stress systematically decreases with increasing strain path change angle, attributed to back-stresses and texture softening for $Ba\langle a\rangle$ slip

[39], twinning in the reload and de-twinning [40]. Our experiments show, however, a significant strengthening in the reload, and twinning is limited. Although the strain path in the 1:1 LPC corresponds to a 90° load strain path change, the different reloading paths result in different deformation behaviors. In our tests the 1:1 proportional load has a forward force component that competes with the back-stresses from the dislocation structure. Thus, dislocations are not free to run backwards and instead act as barriers to forward dislocation motion. The differences in the tests show what advantages cruciforms have over dogbones for approximating real cold-forming processes for sheet metals.

Although most grains are poorly oriented for twinning, some $\{10\bar{1}1\}-\{10\bar{1}2\}$ double twinning and tension twinning is observed. The double twinning is limited to a few grains and is not expected to contribute significantly to the bulk strain. Complex twinning is seen in several grains, such as the one in Fig. 14. In general, the twin variants are selected according to the highest NRSS values. However, some twins, such as the "k" twin in Fig. 14A, nucleate despite having a low NRSS. It is suspected that the nucleation of the "k" twin was aided by high local stresses at the triple junction between the "h", "j", and "i" twins which can overcome the low NRSS [50]. Twin growth is restricted by the high misorientation angles of ~56° at the twin boundaries, which limits the contribution of twinning to the deformation [55,60,62]. Additionally, the twin boundaries act as strong barriers to dislocation due to the high misorientation angles. Dislocation pileups at twin boundaries can act as a forest-hardening mechanism to further dislocation slip and twin growth [23,30,63], making these grains plastically hard. However, there are very few of these grains, so it is expected that the majority of the strengthening is due to dislocation-based hardening in the grains from the preload.

5. Conclusion

For the first time, in-plane tension-tension strain path changes on cold-rolled Mg AZ31B sheet have been investigated *in situ* using neutron diffraction. Post-mortem EBSD was performed to quantify the twinned volume fraction and twin variant selection of the deformation. The findings are summarized below:

1. Acoustic emission during *in situ* deformation of a dogbone sample shows that it is highly unlikely that twinning occurs before microplastic yield (at ~75 MPa for this alloy), as was proposed in Ref. [16].
2. Dogbone and 1:0 monotonic load: Strain is initially accommodated by $Ba\langle a\rangle$ slip and $\{10\bar{1}2\}$ TTW. At higher strains, $Pri\langle a\rangle$ and $Pyr^{2nd}\langle c+a\rangle$ are also active.
3. 7:10 and 1:1 monotonic load: Strain is initially accommodated by $Ba\langle a\rangle$ slip. Twinning is limited to a few grains, implying that $Pyr^{2nd}\langle c+a\rangle$ slip is more active than in the uniaxial loads to accommodate *c*-axis strain. NRSS analysis also suggests that $Pri\langle a\rangle$ slip is limited. When twins are observed, twinning is primarily one- or two-variant $\{10\bar{1}2\}$ TTW and some $\{10\bar{1}1\}-\{10\bar{1}2\}$ double twinning is observed.
4. The dislocation and twin network built up during the 1:0 preload affects the 0:1, 7:10, and 1:1 LPC in different ways:
   a 0:1 LPC (170° strain path change): Back-stresses from the prestrain, de-twinning, and low-CRSS tension twinning and growth result in an undershoot of the force-strain curve. Deformation is dominated by $Ba\langle a\rangle$ slip and high-Schmid variant tension twinning and growth.
   b 7:10 and 1:1 LPC (90° and 135° strain path change): The dislocation network and high-angle twin boundaries from the preload plastically harden the grains, resulting in an overshoot of the force-strain curve. As in the monotonic loads, $Pyr^{2nd}\langle c+a\rangle$ slip is active to accommodate *c*-axis strain in non-twinned grains. NRSS analysis suggests that $Pri\langle a\rangle$ slip is also active in well-oriented grains. Twin nucleation is only observed in a few grains and growth is suppressed by the high angle twin boundaries between different variants.
5. The similar behavior of the 7:10 and 1:1 monotonic load suggest any tensile load that at least prevents contraction in-plane can suppress twinning and promote slip for a strong basal texture. Further multiaxial load experiments should be performed to confirm this behavior.

Acknowledgements

This work was supported by the European Research Council within the ERC Advanced Grant MULTIAX (339245). The authors would like to gratefully acknowledge the ERC for their financial support, as well as the Competence Centre for Materials Science and Technology (CCMX) for their support in the development of the large multiaxial deformation rig. JC acknowledges the financial support of the Czech Science Foundation under the contract 14-36566G.

Appendix A. Supplementary data

Supplementary data to this article can be found online at https://doi.org/10.1016/j.actamat.2018.10.033.

Appendix: Calculation of Normalized Resolved Shear Stress

NRSS derivation

The NRSS values were calculated using Eq. (2) in the main text, Section 2.4. For these calculations, a c/a ratio of 1.624 was used. Stress tensors for the different loads were determined using finite element analysis (details available online as supplementary material). The matrix $\mathbf{g}$ is an orientation matrix that is the product of two rotation matrices $\mathbf{R}_1$ and $\mathbf{R}_2$ which define a rotation to align the lattice plane normal to be parallel to $\mathbf{Q}$ and a rotation around $\mathbf{Q}$, respectively:

$$\mathbf{R}_1 = \mathbf{I} + [\mathbf{v}]_\times + [\mathbf{v}]_\times{}^2\left(\frac{1-\mathbf{b}\cdot\mathbf{Q}}{\mathbf{v}^2}\right) \tag{B.1}$$

$$\mathbf{R}_2 = \begin{bmatrix} \cos\theta + u_1{}^2(1-\cos\theta) & u_1u_2(1-\cos\theta) - u_3\sin\theta & u_1u_3(1-\cos\theta) + u_2\sin\theta \\ u_2u_1(1-\cos\theta) + u_3\sin\theta & \cos\theta + u_2{}^2(1-\cos\theta) & u_2u_3(1-\cos\theta) - u_1\sin\theta \\ u_3u_1(1-\cos\theta) - u_2\sin\theta & u_3u_2(1-\cos\theta) + u_1\sin\theta & \cos\theta + u_3{}^2(1-\cos\theta) \end{bmatrix} \tag{B.2}$$

where $\mathbf{I}$ is the identity matrix, $[\mathbf{v}]_\times$ is the skew matrix of cross product $\mathbf{v} = \mathbf{b} \times \mathbf{Q}$, and $u_1, u_2, u_3 = \mathbf{R}_1\mathbf{n}$. The angle θ was taken from 0 to 360° in steps of 0.1° to account for all possible grain orientations in diffraction condition. For all of the slip deformation modes, the absolute values of the NRSS were used. For the twinning modes, negative NRSSs were set to 0 to take into account irreversibility of shear sense.

References

[1] R.W. Klein, B.W. Williams, J. McKinley, J.R. Einhorn, S.R. Agnew, Exploration of thin-walled magnesium alloy tube extrusion for improved crash performance, in: A. Singh, K. Solanki, M.V. nuel, N.R. Neelameggham (Eds.), Magnesium Technology 2016, John Wiley & Sons, Inc., 2016, pp. 223–228, https://doi.org/10.1002/9781119274803.ch45.

[2] J. Bohlen, M.R. Nürnberg, J.W. Senn, D. Letzig, S.R. Agnew, The texture and anisotropy of magnesium–zinc–rare earth alloy sheets, Acta Mater. 55 (2007) 2101–2112, https://doi.org/10.1016/j.actamat.2006.11.013.

[3] J. Hirsch, T. Al-Samman, Superior light metals by texture engineering: optimized aluminum and magnesium alloys for automotive applications, Acta Mater. 61 (2013) 818–843, https://doi.org/10.1016/j.actamat.2012.10.044.

[4] D.W. Brown, S.R. Agnew, S.P. Abeln, W.R. Blumenthal, M.A.M. Bourke, M.C. Mataya, C. Tomé, S.C. Vogel, The role of texture, temperature and strain rate in the activity of deformation twinning, Mater. Sci. Forum (2005), https://doi.org/10.4028/www.scientific.net/MSF.495-497.1037.

[5] D.W. Brown, S.R. Agnew, M.A.M. Bourke, T.M. Holden, S.C. Vogel, C.N. Tomé, Internal strain and texture evolution during deformation twinning in magnesium, Mater. Sci. Eng., A 399 (2005) 1–12, https://doi.org/10.1016/j.msea.2005.02.016.

[6] S.R. Agnew, Ö. Duygulu, Plastic anisotropy and the role of non-basal slip in magnesium alloy AZ31B, Int. J. Plast. 21 (2005) 1161–1193, https://doi.org/10.1016/j.ijplas.2004.05.018.

[7] S.R. Agnew, D.W. Brown, S.C. Vogel, T. Holden, In-situ measurement of internal strain evolution during deformation dominated by mechanical twinning, Mater. Sci. Forum 404–407 (2002) 747–754, https://doi.org/10.4028/www.scientific.net/MSF.404-407.747.

[8] A. Jain, O. Duygulu, D.W. Brown, C.N. Tomé, S.R. Agnew, Grain size effects on the tensile properties and deformation mechanisms of a magnesium alloy, AZ31B, sheet, Mater. Sci. Eng. A 486 (2008) 545–555, https://doi.org/10.1016/j.msea.2007.09.069.

[9] S.R. Agnew, D.W. Brown, C.N. Tomé, Validating a polycrystal model for the elastoplastic response of magnesium alloy AZ31 using in situ neutron diffraction, Acta Mater. 54 (2006) 4841–4852, https://doi.org/10.1016/j.actamat.2006.06.020.

[10] M.A. Gharghouri, G.C. Weatherly, J.D. Embury, J. Root, Study of the mechanical properties of Mg-7.7at.% Al by in-situ neutron diffraction, Philos. Mag. A 79 (1999) 1671–1695, https://doi.org/10.1080/01418619908210386.

[11] X. Hong, A. Godfrey, W. Liu, A. Orozco-Caballero, J.Q. da Fonseca, Effect of pre-existing twinning on strain localization during deformation of a magnesium alloy, Mater. Lett. 209 (2017) 94–96, https://doi.org/10.1016/j.matlet.2017.07.077.

[12] H. Qiao, S.R. Agnew, P.D. Wu, Modeling twinning and detwinning behavior of Mg alloy ZK60A during monotonic and cyclic loading, Int. J. Plast. 65 (2015) 61–84, https://doi.org/10.1016/j.ijplas.2014.08.010.

[13] H. Wang, S.Y. Lee, M.A. Gharghouri, P.D. Wu, S.G. Yoon, Deformation behavior of Mg-8.5wt.%Al alloy under reverse loading investigated by in-situ neutron diffraction and elastic viscoplastic self-consistent modeling, Acta Mater. 107 (2016) 404–414, https://doi.org/10.1016/j.actamat.2016.01.066.

[14] H. Wang, P.D. Wu, C.N. Tomé, J. Wang, Study of lattice strains in magnesium alloy AZ31 based on a large strain elastic-viscoplastic self-consistent polycrystal model, Int. J. Solid Struct. 49 (2012) 2155–2167, https://doi.org/10.1016/j.ijsolstr.2012.04.026.

[15] C. Ma, A. Chapuis, X. Guo, L. Zhao, P. Wu, Q. Liu, X. Mao, Modeling the deformation behavior of a rolled Mg alloy with the EVPSC-TDT model, Mater. Sci. Eng., A 682 (2017) 332–340, https://doi.org/10.1016/j.msea.2016.11.027.

[16] O. Muránsky, D.G. Carr, M.R. Barnett, E.C. Oliver, P. Šittner, Investigation of deformation mechanisms involved in the plasticity of AZ31 Mg alloy: in situ neutron diffraction and EPSC modelling, Mater. Sci. Eng., A 496 (2008) 14–24, https://doi.org/10.1016/j.msea.2008.07.031.

[17] J. Čapek, K. Máthis, B. Clausen, M. Barnett, Dependence of twinned volume fraction on loading mode and Schmid factor in randomly textured magnesium, Acta Mater. 130 (2017) 319–328, https://doi.org/10.1016/j.actamat.2017.03.017.

[18] K. Máthis, P. Beran, J. Čapek, P. Lukáš, In-situ neutron diffraction and acoustic emission investigation of twinning activity in magnesium, J. Phys.: Conf. Ser. 340 (2012), 012096, https://doi.org/10.1088/1742-6596/340/1/012096.

[19] J. Čapek, K. Máthis, T. Krajšák, The use of acoustic emission and neutron diffraction to reveal the active deformation mechanisms in polycrystalline magnesium and comparison to theoretical modeling, in: A. Singh, K. Solanki, M.V. nuel, N.R. Neelameggham (Eds.), Magnesium Technology 2016, John Wiley & Sons, Inc., 2016, pp. 213–216, https://doi.org/10.1002/9781119274803.ch43.

[20] J. Čapek, K. Máthis, B. Clausen, J. Stráská, P. Beran, P. Lukáš, Study of the loading mode dependence of the twinning in random textured cast magnesium by acoustic emission and neutron diffraction methods, Mater. Sci. Eng., A 602 (2014) 25–32, https://doi.org/10.1016/j.msea.2014.02.051.

[21] B. Song, G. Huang, H. Li, L. Zhang, G. Huang, F. Pan, Texture evolution and mechanical properties of AZ31B magnesium alloy sheets processed by repeated unidirectional bending, J. Alloy. Comp. 489 (2010) 475–481, https://doi.org/10.1016/j.jallcom.2009.09.090.

[22] M. Knezevic, A. Levinson, R. Harris, R.K. Mishra, R.D. Doherty, S.R. Kalidindi, Deformation twinning in AZ31: influence on strain hardening and texture evolution, Acta Mater. 58 (2010) 6230–6242, https://doi.org/10.1016/j.actamat.2010.07.041.

[23] H. El Kadiri, J. Kapil, A.L. Oppedal, L.G. Hector, S.R. Agnew, M. Cherkaoui, S.C. Vogel, The effect of twin–twin interactions on the nucleation and propagation of {1012} twinning in magnesium, Acta Mater. 61 (2013) 3549–3563, https://doi.org/10.1016/j.actamat.2013.02.030.

[24] P. Chen, B. Li, D. Culbertson, Y. Jiang, Contribution of extension twinning to plastic strain at low stress stage deformation of a Mg-3Al-1Zn alloy, Mater. Sci. Eng., A 709 (2018) 40–45, https://doi.org/10.1016/j.msea.2017.10.038.

[25] L. Lv, Y. Xin, H. Yu, R. Hong, Q. Liu, The role of dislocations in strain hardening of an extension twinning predominant deformation, Mater. Sci. Eng., A 636 (2015), https://doi.org/10.1016/j.msea.2015.04.007.

[26] S.R. Agnew, O. Duygulu, Tem investigation of dislocation mechanisms in Mg alloy AZ31B sheet, in: Magnesium Technology, 2004.

[27] A.L. Oppedal, H.E. Kadiri, C.N. Tomé, S.C. Vogel, M.F. Horstemeyer, Anisotropy in hexagonal close-packed structures: improvements to crystal plasticity approaches applied to magnesium alloy, Phil. Mag. 93 (2013) 4311–4330, https://doi.org/10.1080/14786435.2013.827802.

[28] A.L. Oppedal, H. El Kadiri, C.N. Tomé, G.C. Kaschner, S.C. Vogel, J.C. Baird, M.F. Horstemeyer, Effect of dislocation transmutation on modeling hardening mechanisms by twinning in magnesium, Int. J. Plast. 30–31 (2012) 41–61, https://doi.org/10.1016/j.ijplas.2011.09.002.

[29] F. Wang, S. Agnew, Dislocation-twin interactions in magnesium alloy AZ31, in: Magnesium Technology 2015, Springer, Cham, 2015, pp. 139–144, https://doi.org/10.1007/978-3-319-48185-2_27.

[30] F. Wang, S.R. Agnew, Dislocation transmutation by tension twinning in magnesium alloy AZ31, Int. J. Plast. 81 (2016) 63–86, https://doi.org/10.1016/j.ijplas.2016.01.012.

[31] H. Qiao, X.Q. Guo, A.L. Oppedal, H. El Kadiri, P.D. Wu, S.R. Agnew, Twin-induced hardening in extruded Mg alloy AM30, Mater. Sci. Eng., A 687 (2017) 17–27, https://doi.org/10.1016/j.msea.2016.12.123.

[32] X.Y. Lou, M. Li, R.K. Boger, S.R. Agnew, R.H. Wagoner, Hardening evolution of AZ31B Mg sheet, Int. J. Plast. 23 (2007) 44–86, https://doi.org/10.1016/j.ijplas.2006.03.005.

[33] R.H. Wagoner, X.Y. Lou, M. Li, S.R. Agnew, Forming behavior of magnesium sheet, J. Mater. Process. Technol. 177 (2006) 483–485, https://doi.org/10.1016/j.jmatprotec.2006.04.121.

[34] Y. Chino, K. Kimura, M. Mabuchi, Deformation characteristics at room temperature under biaxial tensile stress in textured AZ31 Mg alloy sheets, Acta Mater. 57 (2009) 1476–1485, https://doi.org/10.1016/j.actamat.2008.11.033.

[35] D. Steglich, Y. Jeong, M.O. Andar, T. Kuwabara, Biaxial deformation behaviour of AZ31 magnesium alloy: crystal-plasticity-based prediction and experimental validation, Int. J. Solid Struct. 49 (2012) 3551–3561, https://doi.org/10.1016/j.ijsolstr.2012.06.017.

[36] R.A. Lebensohn, C.N. Tomé, A self-consistent anisotropic approach for the simulation of plastic deformation and texture development of polycrystals: application to zirconium alloys, Acta Metall. Mater. 41 (1993) 2611–2624, https://doi.org/10.1016/0956-7151(93)90130-K.

[37] R.A. Lebensohn, C.N. Tomé, P.P. CastaÑeda, Self-consistent modelling of the mechanical behaviour of viscoplastic polycrystals incorporating intragranular field fluctuations, Phil. Mag. 87 (2007) 4287–4322, https://doi.org/10.1080/14786430701432619.

[38] H. Zhang, G. Huang, J. Fan, H.J. Roven, B. Xu, H. Dong, Deep drawability and drawing behaviour of AZ31 alloy sheets with different initial texture, J. Alloy. Comp. 615 (2014) 302–310, https://doi.org/10.1016/j.jallcom.2014.06.199.

[39] W. Wen, M. Borodachenkova, C.N. Tomé, G. Vincze, E.F. Rauch, F. Barlat, J.J. Grácio, Mechanical behavior of Mg subjected to strain path changes: experiments and modeling, Int. J. Plast. 73 (2015) 171–183, https://doi.org/10.1016/j.ijplas.2014.10.009.

[40] T. Hama, Y. Tanaka, M. Uratani, H. Takuda, Deformation behavior upon two-step loading in a magnesium alloy sheet, Int. J. Plast. 82 (2016) 283–304, https://doi.org/10.1016/j.ijplas.2016.03.009.

[41] S. Van Petegem, J. Wagner, T. Panzner, M.V. Upadhyay, T.T.T. Trang, H. Van Swygenhoven, In-situ neutron diffraction during biaxial deformation, Acta Mater. 105 (2016) 404–416, https://doi.org/10.1016/j.actamat.2015.12.015.

[42] N. Deng, T. Kuwabara, Y.P. Korkolis, Cruciform specimen design and verification for constitutive identification of anisotropic sheets, Exp. Mech. 55 (2015) 1005–1022, https://doi.org/10.1007/s11340-015-9999-y.

[43] M.V. Upadhyay, T. Panzner, S.V. Petegem, H.V. Swygenhoven, Stresses and strains in cruciform samples deformed in tension, Exp. Mech. 57 (2017) 905–920, https://doi.org/10.1007/s11340-017-0270-6.

[44] U. Stuhr, M. Grosse, W. Wagner, The TOF-strain scanner POLDI with multiple frame overlap—concept and performance, Mater. Sci. Eng., A 437 (2006) 134–138, https://doi.org/10.1016/j.msea.2006.04.069.

[45] U. Stuhr, H. Spitzer, J. Egger, A. Hofer, P. Rasmussen, D. Graf, A. Bollhalder,

M. Schild, G. Bauer, W. Wagner, Time-of-flight diffraction with multiple frame overlap Part II: the strain scanner POLDI at PSI, Nucl. Instrum. Methods Phys. Res. Sect. A Accel. Spectrom. Detect. Assoc. Equip. 545 (2005) 330–338, https://doi.org/10.1016/j.nima.2005.01.321.

[46] O. Arnold, J.C. Bilheux, J.M. Borreguero, A. Buts, S.I. Campbell, L. Chapon, M. Doucet, N. Draper, R. Ferraz Leal, M.A. Gigg, V.E. Lynch, A. Markvardsen, D.J. Mikkelson, R.L. Mikkelson, R. Miller, K. Palmen, P. Parker, G. Passos, T.G. Perring, P.F. Peterson, S. Ren, M.A. Reuter, A.T. Savici, J.W. Taylor, R.J. Taylor, R. Tolchenov, W. Zhou, J. Zikovsky, Mantid—data analysis and visualization package for neutron scattering and SR experiments, Nucl. Instrum. Methods Phys. Res. Sect. A Accel. Spectrom. Detect. Assoc. Equip. 764 (2014) 156–166, https://doi.org/10.1016/j.nima.2014.07.029.

[47] E. Pomponi, A. Vinogradov, A real-time approach to acoustic emission clustering, Mech. Syst. Signal Process. 40 (2013) 791–804, https://doi.org/10.1016/j.ymssp.2013.03.017.

[48] S.V. Petegem, A. Guitton, M. Dupraz, A. Bollhalder, K. Sofinowski, M.V. Upadhyay, H.V. Swygenhoven, A miniaturized biaxial deformation rig for in situ mechanical testing, Exp. Mech. 57 (2017) 569–580, https://doi.org/10.1007/s11340-016-0244-0.

[49] J.J. Jonas, S. Mu, T. Al-Samman, G. Gottstein, L. Jiang, È. Martin, The role of strain accommodation during the variant selection of primary twins in magnesium, Acta Mater. 59 (2011) 2046–2056, https://doi.org/10.1016/j.actamat.2010.12.005.

[50] S. Mu, J.J. Jonas, G. Gottstein, Variant selection of primary, secondary and tertiary twins in a deformed Mg alloy, Acta Mater. 60 (2012) 2043–2053, https://doi.org/10.1016/j.actamat.2012.01.014.

[51] W. Wu, H. Qiao, K. An, X. Guo, P. Wu, P.K. Liaw, Investigation of deformation dynamics in a wrought magnesium alloy, Int. J. Plast. 62 (2014) 105–120, https://doi.org/10.1016/j.ijplas.2014.07.005.

[52] P.D. Wu, X.Q. Guo, H. Qiao, S.R. Agnew, D.J. Lloyd, J.D. Embury, On the rapid hardening and exhaustion of twinning in magnesium alloy, Acta Mater. 122 (2017) 369–377, https://doi.org/10.1016/j.actamat.2016.10.016.

[53] H. Wang, B. Raeisinia, P.D. Wu, S.R. Agnew, C.N. Tomé, Evaluation of self-consistent polycrystal plasticity models for magnesium alloy AZ31B sheet, Int. J. Solid Struct. 47 (2010) 2905–2917, https://doi.org/10.1016/j.ijsolstr.2010.06.016.

[54] S. Mu, T. Al-Samman, V. Mohles, G. Gottstein, Cluster type grain interaction model including twinning for texture prediction: application to magnesium alloys, Acta Mater. 59 (2011) 6938–6948, https://doi.org/10.1016/j.actamat.2011.07.045.

[55] M.A. Kumar, I.J. Beyerlein, R.J. McCabe, C.N. Tomé, Grain neighbour effects on twin transmission in hexagonal close-packed materials, Nat. Commun. 7 (2016) 13826, https://doi.org/10.1038/ncomms13826.

[56] L. Wu, S.R. Agnew, D.W. Brown, G.M. Stoica, B. Clausen, A. Jain, D.E. Fielden, P.K. Liaw, Internal stress relaxation and load redistribution during the twinning–detwinning-dominated cyclic deformation of a wrought magnesium alloy, ZK60A, Acta Mater. 56 (2008) 3699–3707, https://doi.org/10.1016/j.actamat.2008.04.006.

[57] G. Proust, C.N. Tomé, A. Jain, S.R. Agnew, Modeling the effect of twinning and detwinning during strain-path changes of magnesium alloy AZ31, Int. J. Plast. 25 (2009) 861–880, https://doi.org/10.1016/j.ijplas.2008.05.005.

[58] L. Wu, S.R. Agnew, Y. Ren, D.W. Brown, B. Clausen, G.M. Stoica, H.R. Wenk, P.K. Liaw, The effects of texture and extension twinning on the low-cycle fatigue behavior of a rolled magnesium alloy, AZ31B, Mater. Sci. Eng. A 527 (2010) 7057–7067, https://doi.org/10.1016/j.msea.2010.07.047.

[59] M. Arul Kumar, I.J. Beyerlein, C.N. Tomé, Grain size constraints on twin expansion in hexagonal close packed crystals, J. Appl. Phys. 120 (2016) 155105, https://doi.org/10.1063/1.4965719.

[60] S.-G. Hong, S.H. Park, C.S. Lee, Strain path dependence of {10−12} twinning activity in a polycrystalline magnesium alloy, Scripta Mater. 64 (2011) 145–148, https://doi.org/10.1016/j.scriptamat.2010.09.030.

[61] L. Capolungo, I.J. Beyerlein, C.N. Tomé, Slip-assisted twin growth in hexagonal close-packed metals, Scripta Mater. 60 (2009) 32–35, https://doi.org/10.1016/j.scriptamat.2008.08.044.

[62] A. Khosravani, D.T. Fullwood, B.L. Adams, T.M. Rampton, M.P. Miles, R.K. Mishra, Nucleation and propagation of {1012} twins in AZ31 magnesium alloy, Acta Mater. 100 (2015) 202–214, https://doi.org/10.1016/j.actamat.2015.08.024.

[63] M.H. Yoo, Slip, twinning, and fracture in hexagonal close-packed metals, in: MTA 12, 1981, pp. 409–418, https://doi.org/10.1007/BF02648537.